Optimization and Parametric Characterization of a Hydrodynamic Microvortex Chip for Single Cell Rotation

by

Rishabh M. Shetty

A Thesis Presented in Partial Fulfillment
of the Requirements for the Degree
Master of Science

Approved June 2013 by the
Graduate Supervisory Committee:

Deirdre R. Meldrum, Chair
Roger H. Johnson
Stephen Helms Tillery

ARIZONA STATE UNIVERSITY

August 2013

ABSTRACT

Volumetric cell imaging using 3D optical Computed Tomography (cell CT) is advantageous for identification and characterization of cancer cells. Many diseases arise from genomic changes, some of which are manifest at the cellular level in cytostructural and protein expression (functional) features which can be resolved, captured and quantified in 3D far more sensitively and specifically than in traditional 2D microscopy. Live single cells were rotated about an axis perpendicular to the optical axis to facilitate data acquisition for functional live cell CT imaging. The goal of this thesis research was to optimize and characterize the microvortex rotation chip. Initial efforts concentrated on optimizing the microfabrication process in terms of time (6-8 hours v/s 12-16 hours), yield (100% v/s 40-60%) and ease of repeatability. This was done using a tilted exposure lithography technique, as opposed to the backside diffuser photolithography (BDPL) method used previously (Myers 2012) (Chang and Yoon 2004). The fabrication parameters for the earlier BDPL technique were also optimized so as to improve its reliability. A new, PDMS to PDMS demolding process (soft lithography) was implemented, greatly improving flexibility in terms of demolding and improving the yield to 100%, up from 20-40%.

A new pump and flow sensor assembly was specified, tested, procured and set up, allowing for both pressure-control and flow-control (feedback-control) modes; all the while retaining the best features of a previous, purpose-built pump assembly. Pilot experiments were performed to obtain the flow rate regime required for cell rotation.

These experiments also allowed for the determination of optimal trapezoidal neck widths (opening to the main flow channel) to be used for cell rotation characterization. The optimal optical trap forces were experimentally estimated in order to minimize the required optical power incident on the cell. Finally, the relationships between (main channel) flow rates and cell rotation rates were quantified for different trapezoidal chamber dimensions, and at pre-determined constant values of laser trapping strengths, allowing for parametric characterization of the system.

DEDICATION

I dedicate this thesis to my parents Sabita M. Shetty and Manoj R. Shetty, without whom I would have never been who I am and where I am today. I would also like to dedicate this to all my angels, on earth and in heaven who have constantly guided and supported me through everything I have ever done in my life.

TABLE OF CONTENTS

Page

LIST OF TABLES

LIST OF FIGURES

Figure Page

Figure Page

1. INTRODUCTION

1.1 Single cell analysis

Single cell analysis (SCA) has been gaining wide recognition and popularity in the last few years and has become a key technology in our efforts to better understand cellular functions. Phenotype distributions among a cell population's members are not accessible through bulk measurements. A popular approach has therefore been miniaturization of established engineering and cell biological practices and concepts so as to match the dimensions of single cells to enable their interrogation as individuals. Over the years a number of methods have been developed to conduct invasive (chemical) and non-invasive (biological) SCA using innovative microfluidics and microreactor concepts. Recently, SCA 'omics approaches are being more frequently used as tools for systems biology, genomics, transcriptomics, proteomics, metabolic engineering and bioprocess optimization (Fritzsch et al. 2012).

The necessity for single cell analysis stems from the now widely-appreciated notion that the behaviors of important and interesting subpopulations can be masked in bulk-cell, averaged measurements; which in effect, blinds researchers to what could possibly constitute breakthrough insights and discoveries. Heterogeneity among cell populations plays an important role in diseases like cancer, and in resistance to its treatment. Therefore, SCA is recognized as an important field of study (De Souza 2011; Lidstrom and Meldrum 2003). The power of SCA is evidenced by this example: "Consider a bimodal distribution of a specific compound in a cell line, such as a high- and low-copy-

number expression of a specific protein. An ensemble method would detect a mean value masking the bimodal distribution within the cell ensemble. However, analyzing individual cells could resolve two subpopulations—one with high and another with low copy numbers—thus revealing the two different states of expression levels. This simple example can be amplified to more complicated and relevant questions of biological importance, such as the different states during differentiation, proliferation or disease and different responses to external stimuli and intracellular reactions" (Di Carlo & Lee, 2006).

SCA tools enable the study of dynamics at the single-cell level and provide access to the investigation of subcellular compartments. One difficulty in SCA is presented by the requirement to manipulate micron scale objects. Analytes of interest can be extremely complex and are usually available in minute amounts (Stone et al. 2004; Squires & Quake 2005), providing challenges in obtaining sufficient signal-to-noise ratios (SNR). Microfluidic or lab-on-a-chip devices have been the method of choice for SCA tools because they allow for easy integration of some of the most basic and necessary steps of SCA such as separation, selection and positioning of target cells; and possibly lysis, separation and detection of the particular cellular analytes of interest. In cases where it is advantageous, microfluidic devices allow cells to be confined in compartments in or near their own intrinsic microenvironments, chemically isolated from their neighbors. This can help reduce dilution effects and can also increase detection sensitivity (T.-C. Chao and Ros 2008; Gao, Zhang, and Meldrum 2011; S.-H. Chao et al. 2007; Molter et al. 2008).

Lab-on-chip devices offer avenues to improve performance and throughput and provide opportunities for parallelization and automation. Microfluidic systems possess some inherent unique and advantageous attributes due to the physics of scale. For instance, they generally have low Reynolds numbers, which assures laminar flow conditions, and mass transport is diffusion dominated, providing significant advantages for mixing and dispersion, especially for live cells (Stone et al. 2004; Squires & Quake 2005). One of the most important applications of SCA is in the field of cancer research. Cancer tumors are not a monotonous mass of identical cells with uniform behaviors, but exhibit a substantial degree of heterogeneity. Cells can act quite differently in one part of a tumor than in another. For instance, genes critical to cell proliferation may be active in one area but not in another. A subpopulation of tumor cells may be dormant, rendering them effectively invisible to targeted therapy. This heterogeneity lies at the root of treatment failures and is partially to blame for the difficulty in identifying better diagnostic and prognostic markers for the disease. By studying single cells in their microenvironments, information about particularly interesting cell lines (K562 leukemia cells in our case) and their phenotypes can be obtained (NCI Cancer Bulletin,Vol 9/Number 18, 2012**).** (Avery 2006) (Zeng et al. 2011). (Cohen et al. 2008). Studies that probe intercellular variability are therefore critical in understanding how alterations in cell phenotypes often result in a selective advantage of some cells over others in the same population (Losick and Desplan 2008). These studies may also reveal the details behind cell fate decisions and how cancer cells acquire the ability to evade contact inhibition and programmed cell death, or death resulting from an external stimulus such as radiation or drugs.

1.1.1 Single cell imaging

While both live and fixed cell imaging can elucidate cell biological information, the former is quite attractive since it facilitates the capture of dynamic and transient events like apoptosis in a single cell. Deregulated apoptosis has been implicated in diverse pathologies including cancer and certain neurodegenerative diseases. Some of these apoptotic events include mitochondrial outer membrane permeabilization (MOMP), mitochondrial dysfunction, phosphatidylserine exposure and membrane permeabilization (Tait et al. 2009). The defining morphological characteristics of apoptosis include cell shrinkage, nuclear fragmentation, chromatin condensation and membrane blebbing (Tait and Green 2010).

Imaging technologies have been adapting and advancing in order to keep up with the demanding nature of SCA studies. Optical microscopy has myriad applications in biological research and clinical practice. Three-dimensional (3D) measurements are required because cells and tissues have complex shapes and structures (Miao et al. 2012). Multimodal microscopes that combine absorption and immunofluorescence (IF) contrast mechanisms have been developed to allow cytopathologists who rely on absorption-based stains such as hemotoxylin and eosin (H&E) to acclimatize easily to advancements made possible by IF (Glasbey & Martin 1996). Optical projection tomographic microscopy (OPTM) can provide 3D absorption and fluorescence images with isometric resolution (Fauver et al. 2005). In OPTM, now called cell computed tomography (cell CT), a high

NA objective's focal plane is scanned axially through the sample to create an extended depth of field (DOF) image which is mathematically similar to a projection image in conventional x-ray or emission CT. The cell CT technique has led to the development of specialized instruments referred to as optical cell-CT (Miao et al. 2012). Introduction of 3D imaging into the field of cytology and pathology has allowed access to quantitative information of diagnostic, prognostic and therapeutic value, and provided the capacity for automated image analysis and disease state classification, thereby eliminating diagnostic variability between cytopathologists, cytotechnicians and pathologists. Cell-CT's 3D images offer a threefold reduction in false negative rates for adenocarcinoma detection compared to that provided by 2D images, at the same high 96% specificity (Meyer et al. 2009). In the current cell-CT (VisionGate Inc., Phoenix, AZ) fixed cells are suspended in a refractive index-matching gel and rotated in a microcapillary, while a piezoelectric-driven, high magnification objective lens scans through the extent of the cell volume (Fauver et al. 2005). Although this method offers isotropic spatial resolution of 150 nm and improves cell classification performance relative to slide-based cytology (Meyer et al., 2009) (Nandakumar et al. 2011), no live-cell compatible version of it is available to date. A live-cell CT would facilitate dynamic interrogation of protein-protein interactions and a powerful array of other cell biological studies.

A particular far-field fluorescence microscopy technique which takes advantage of the photophysical properties of fluorescent molecules, extends the available spatial information to the cellular and molecular scale. This method of live-cell 3D super

resolution imaging can achieve a lateral localization precision of < 35 nm and an axial localization accuracy of 65-140 nm depending on sample characteristics (Zanacchi et al. 2011).

As the name suggests, a hybrid technique called correlative light and electron microscopy (EM) uses both, light microscopy (phase-contrast or fluorsescence on living or fixed samples) and electron microscopy (immuno EM, scanning EM, transmission EM, cryo EM and EM tomography) to visualize the same object. The method uses laser pre-micro-patterned aclar disks as culture substrates. These substrates are compatible with cryofixation and resin embedding. The regions of interest (ROIs) selected during the live cell imaging phase can be conserved throughout the preparation steps for EM and used to study phenomena such as cell migration (time-lapse recordings). While light microscopy provides access to the functional state of a given protein or cell under physiological conditions, EM enables a precise localization of the same protein or cell at higher resolution (Spiegelhalter et al. 2010).

Mathematically, the resolution equation (Verdet 1869; Abbe 1873; Rayleigh 1896) states that 'the resolution of a light microscope is limited to $\lambda/[2n\sin\alpha]$ in the focal plane (xy) and $2/[n\sin^2\alpha]$ along the optical axis (z), where the wavelength of the light is used, n is the refractive index, and $[n\sin\alpha]$ is the numerical aperture of the lens'. Because the majority of lenses have a numerical aperture of <1.5 (α is <70°), the common resolution limit for cell imaging is 150 nm laterally (within the focal plane) and 500 nm along the

optical axis. However, because sub-resolution emitters can be detected, if not technically resolved, by fluorescence microscopes, an increasing number of studies are showing that fluorescence light microscopy has developed into ‘nanoscopy’, revolutionizing the view of cellular and subcellular life. Researchers exploiting a variety of super-resolution techniques are now able to analyze large data sets of digital images and produce high-fidelity, high resolution (on the order of 50-100 nm spatial resolution) 3D imagery (Hell and Stelzer 1992; Schrader and Hell 1996; Betzig et al. 2006; Gustafsson 2008; Gustafsson et al. 2008; Huang et al. 2008; Lippincott-Schwartz and Manley 2009). Overcoming the diffraction limit has made it possible to observe and record dynamic events as they occur and even visualize protein–protein interactions and single molecules in living cells. Electron microscopy, with Angstrom-order resolution, provides near-atomic-level details, but is not amenable to live-cell imaging (K. Cortese, Diaspro, and Tacchetti 2009).

By saturating fluorophore transitions, optical nanoscopy has been able to provide image resolution at the sub-diffraction-limited scale, and has been demonstrated to work well with certain fluorescent proteins. Sub-diffraction resolution has also been obtained with saturated fluorescence using marker free and time-lapse nanoscopy. This method demonstrates the ability to provide less than 100 nm lateral and about 150 nm axial resolution (Cotte et al. 2013)**.**

Another method to overcome the anisotropic resolution and axial aberration is, similar to cell CT, rotating the cell around an axis perpendicular to the optical (z) axis, allowing the microscope optics to take advantage of their higher lateral resolving power. Light reconstruction from z-stacks acquired from the same cell, but taken from different angled viewpoints while the cell is rotating, significantly improves resolution and can be used to obtain 'tomographic' information about the cell, thus allowing a true 3D representation of the cell on reconstruction (Heintzmann & Cremer, 2002; Swoger et al., 2007; Renaud et al., 2008; Le Saux et al. 2009). Imaging live, single cells while rotating them can be a powerful tool for obtaining information about important events in cancer metabolism and protein-protein relationships and protein-nucleic acid interactions. It is critical to appreciate their spatial relationships and to provide this sort of information over a time course of minutes to hours.

1.2 Methods for single cell manipulation and rotation

Ever since the mid-1900s, in addition to observation of stationary particles, scientists and engineers had a strong interest in techniques which could manipulate cells and other biological particles. A photo-electric device to continuously count flowing cells (possibly the first description of a flow cytometer) was reported in 1934 (Moldavan 1934). Thereafter, the concept of hydrodynamic focusing of cells into a single-file stream, as introduced by Crossland-Taylor in the mid-1950s, made it possible to accurately manipulate and deliver cells suspended in a fluid within narrow capillaries (Crossland-Taylor 1953). Arthur Ashkin at Bell Laboratories first reported the concept of an optical

trapping technique which could manipulate single cells (Ashkin 1970), and he and his colleagues demonstrated trapping and manipulation of viruses and bacteria using a tightly focused laser beam (Ashkin 1987).

Important advances have been made recently in the lab-on-a-chip field, which applies microfluidic techniques and devices for new applications in the fields of molecular biology, genetic analysis and proteomics, and these have contributed to the advancement of single cell analysis and mechanistic understanding. Various cell manipulation techniques in microfluidics have been developed to meet the demands of specific research objectives (H. Yun, Kim, and Lee 2013). Methods applying external forces for microparticle manipulation can be categorized as:

- Optical techniques
- Magnetic techniques
- Electrical techniques and
- Mechanical techniques

A brief description of the basic principles, methods and applications of these five categories follows.

1.2.1 Optical manipulation

Optical trapping can be achieved using a laser beam (generally near-infrared in the 800- to 1100-nm region), focused through a high numerical aperture (NA) objective lens on a microscope. The technique uses differences between a gradient and a scattering optical

force to either attract and trap, or repel, a target particle. These forces depend on the wavelength of the laser beam (λ) and the particle size (r). If the gradient force exceeds the scattering force on the particle of interest, the particle can be trapped at the near focal point of the objective lens (H. Yun, Kim, and Lee 2013). In essence, the laser beam carries a momentum that is transferred to the cell or particle of interest when the beam interacts with it. The more Gaussian the profile of the beam, the better the trapping of the object and the more tightly focused the beam is and the easier it is to trap the particle in the direction of the laser beam (along the optical, or z, axis) (Nilsson et al. 2009). Once the object is trapped, it can be manipulated in all dimensions by moving the laser beam and changing its focus. The optical system can be calibrated to measure the forces exerted on the trapped object (generally in the hundred-pN range) (Moffitt et al. 2008). The sizes of the particles that can be trapped range from a few Angstroms up to 10 μm or more. Cell trapping occurs in the Mie regime ($r >> \lambda$) where the particle size is larger than the wavelength of the irradiation light. Both the magnitude and the direction of the forces depend on the particle shape, and trapping is generally restricted to spheres and ellipsoids (Zhang and Liu 2008) (Ashkin & Dziedzic 1987; Ashkin 2007).

In order to manipulate intracellular structures like the nucleus in a living cell, small lipid granules can be trapped optically and used as a handle to exert a pushing force on the cell nucleus (Sacconi et al. 2005). Optical manipulation techniques to introduce membrane-impermeable molecules into living cells have significant implications for cell biological research and medical applications. They are also useful for cell deformability analysis (Lee et al. 2007) (Lee, Demirci, Khademhosseini 2009). An optical cell rotator (OCR),

which uses an asymmetric dual-beam laser trap for trapping and inducing a controlled rotation of the cell by means of counter-propagating divergent laser beams, has been proposed for tomographic microscopy in 3D cell imaging (Kreysing et al. 2008). Another method uses a spatial light modulator to create a pair of closely separated traps which apply force to different parts of the same object. These traps can be made to revolve around each other in any plane of interest, causing the object to rotate about the axis defined by their motion due to the optical torque applied (Bingelyte et al. 2003).

Studies on radiation damage reveal that IR laser diodes can reduce the optical absorption by the cell, and that the power used to create a given trapping force can be lowered relative to that required when gas discharge lasers such as argon lasers are used (Nilsson et al. 2009). The least harmful wavelengths are 830 and 970 nm, while the region between 870 and 910 nm is particularly damaging and should be avoided. To improve cell viability and increase longevity, it is also suggested that, wherever possible, scavengers or other means should be employed to reduce the oxygen tension in trapping environments (Neuman et al. 1999) (Cheng, Hou and Ye 2010).

1.2.2 Magnetic manipulation

Magnetic manipulation techniques have three broad fields of application- cell separation, on-chip sample preparation and tweezing setups for cell rotation. These techniques utilize either intrinsic properties such as the iron-containing hemoglobin in erythrocytes or external labels such as magnetic nanoparticles attached to cells; for the manipulation of

biological particles using electromagnets or permanent magnets (Melville et al. 1975). In the field of cell separation, the magnetic-activated cell sorting (MACS) is the most popular technique and it uses magnetic nanoparticles conjugated antibodies targeting particular cell surface antigens. Magnetic labeling (MACS) is preferred over the FACS technique which uses fluorescent labeling, as a more effective and affordable tool for high-throughput cell separation (Miltenyi et al. 1990). Magnetic manipulation can be helpful for integrating on-chip sample preparation in microfluidic devices more systematically owing to the ability to hold and release cells easily (Yun, Kim, and Lee 2013). A microfluidic device has been developed to generate a strong induced magnetic field using an array of nickel micro-pillars (Yun et al. 2010; Pamme 2006). This device has been designed to capture target cancer cells by using on-chip sample preparation (Liu et al. 2007). Magnetic tweezers operating in different modes have been used to allow easy rotary motion of bioparticles around the optical axis at approximately 10 Hz, using forces ranging from 50fN to 20pN. They are a low-cost and biocompatible setup and could become a good alternative to other micromanipulators (Gosse and Croquette 2002).

1.2.3 Electrical manipulation

Electrical manipulation usually employs the technique of dielectrophoresis (DEP) i.e. the motion of dielectric particles induced by a non-uniform electric field (Pohl 1951). This motion is determined by the magnitude and polarity of electrical charge on the particles of interest (Jones 2003). As a result, cells can be manipulated either in the direction of increasing field (positive DEP) or decreasing electric field (negative DEP).

DEP has been a powerful technique in microfluidic applications such as isolation, positioning, patterning and separating target cells based on their dielectric properties (Doh and Cho 2005). A dielectric affinity column can be used to trap large cancer cells on the electrode tips by the DEP field, while smaller blood cells escape. A micro-cytometer using DEP to produce noncontact single-cell traps has been devised (Sivagnanam et al. 2010). Using non-uniform electric fields produced in DEP, polarizable microparticles such as cells can be manipulated while being suspended in liquid culture media. Using a rotating electric field between quadrupoles (4 electrodes), octopoles (8 electrodes) and other configurations, a controlled cell rotation can be induced in cells at different frequencies and voltages. MEMS (microelectromechanical systems) based fabrication techniques are used to pattern these electrodes on substrates. A cell is delivered into a sample chamber where the non-uniform electric fields are first used for trapping and then rotating the cell (Schnelle et al. 2003; Shorte et al. 1993). This technique has been used to reconstruct high resolution 3D images of cells based on z-stack images obtained while the cell is spinning around an axis perpendicular to the optical axis. During the micro-rotation induced by the modulated field in the cage, image slices are taken at a predetermined rate, dependent on the cell rotation rate (Le Saux et al. 2009). By obtaining a large number of images at different and closely spaced angles, the anisotropy problem of microscopic resolution can be overcome (Yu et al. 2011).

1.2.4 Mechanical manipulation

Early flow cytometry techniques using a capillary tube for flowing cells faced the problem that the device could not measure meaningful cell-signals. Capillary blocking and interference of signals were observed, due to narrow tubes (Moldavan 1934). When wider tubes were used, there was a problem with coincidence detection of multiple cells, owing to the sheer number of cells that the tubes let through. To overcome this problem, the hydrodynamic cell manipulation technique was developed (Crossland-Taylor 1953), which allowed the cells to be aligned in a single line, using a sheath fluid. This enabled particle positioning regardless of the size of particles, minimizing unwanted clogging of the manipulation apparatus. In addition, optimal optical interrogation, higher precision and high-throughput have all been achieved (Yun, Kim, and Lee 2013).

High throughput single cell manipulation can be achieved using microfluidics. One approach for precisely manipulating microparticles is to use mobile microvortices at low Reynolds numbers (10^{-1} to 10^{-4}). These microvortices can be generated by the rotation of magnetic microactuators such as nickel nanowires or self-assembled magnetic bead doublets in the fluid. The center of the microvortex is the site of a trapping force, which is locally induced by the flow velocity gradient in that region. Using a weak rotating magnetic field as an energy source ($|B| < 5$ mT), the amplitude and position of the microvortex can be controlled to selectively trap and transport microparticles, (Petit et al. 2012). Another similar idea demonstrates hydrodynamic trapping of bioparticles in a microfluidic device using a resonating micro plate driven by Lorentz force. This

approach can generate two counter-rotating microvortices (Lin et al. 2008). Yet another method using microvortices is aimed at making available a scalable and low-cost device for focusing and/or separating a variety of cell types and particles, by tuning the density of the medium (Hsu et al. 2008).

One way of rotating single cells about an axis parallel to the optical axis (2D rotation) using microvortices is to fabricate channels with diamond shaped side chambers. This would allow flow to be peeled off from the main channel and become recirculant in the side channel, thus forming a microvortex (Lim et al. 2003). The dimensions of the opening chamber and especially its opening angle and aspect ratio are important factors that decide how stable the microvortex is. To exert better control on the cells during rotation, an optical trap was used to position the cell at the center of the microvortex. Thereafter, the shear stress from the recirculant flow in the microvortex caused the rotation of the cell (Chiu 2007). A spinning cell could be retained without significant damage or loss of trapping up to an estimated 200 Hz. A calculation of the radial acceleration from average flow rates in the micro channel shows that only about 20% of the average flow velocity in the channel is converted to rotational velocity in the cavity of the rotation chamber (Shelby and Chiu 2004).

In order to use this method to rotate cells about an axis perpendicular to the optical axis, a sub-channel chamber is needed and this can be micro fabricated in the form of a trapezoid. The trapezoidal feature is able to generate the recirculant flow to produce a

microvortex for single cell rotation. This technique is suitable for imaging of cells once stable rotation enables confocal z-stack imaging of live single cells, or better yet, true isotropic 3D imaging via live cell CT.

1.3 Fabrication of trapezoidal features/undercut structures

Wet etching, whether isotropic or anisotropic has been the method of choice in the past for microfabrication of undercut structures. Some examples of wet etching are KOH etching of silicon (100) to obtain anisotropic structures (M. H. Yun 1998) and HF etching of glass for isotropic structures (Berthold et al. 2000).

Recently, several fabrication methods for obtaining 3D microstructures such as micro-stereo lithography (Ikuta, Maruo, Kojima 1998), grayscale lithography (Suleski and O'Shea 1995; O'Shea and Rockward 1995), multi-exposure and single development (MESD) technique (Yoon et al. 1998), inclined/tilted UV lithography (Beuret, Racine, and Centre 2007); (Baek and Song 2011) and 3D diffuser lithography (Chang and Yoon 2004); Jeon et al. 2007) have been introduced. The last two methods are the ones used for this thesis work as they lend themselves suitably to the fabrication of undercut structures. Inclined backside UV lithography (using a block of the required tilt angle) can be extremely effective and easy to use and repeat. This method has several advantages over the backside diffuser method discussed in Chapter 2. This inclined backside UV lithography method was used to fabricate trapezoidal sub-channel chambers.

1.4 Background information on simulations

Results from the previously executed COMSOL Multiphysics v4.2a (COMSOL Inc.) simulations (Myers 2012) are summarized here:

- A critical requirement of the cell rotation imaging apparatus (an inverted microscope) is that the trapping chamber be flat backed (i.e. have its bottom side parallel to the flow channel in a cross-sectional view). The flat bottomed trapezoidal sub-channel chamber was the only one that would allow vortices to be formed while also allowing interference-free imaging. The amount of flow detached from the main channel is dependent upon the angle of incidence, the (angle between the main flow channel and opening neck of the trapezoid. As the angle of incidence increased, the amount of flow detached decreased (thus forming weaker vortices). The displacement of the center of the vortex from the chamber inlet was close to 18 μm irrespective of the incident angle (30º, 60º and 90º tested). This displacement was dependent instead on the aspect ratio (feature height/inlet width) and was higher on either side of an aspect ratio of 1 (say, 0.5 and 1.5). This meant that features with aspect ratios of 0.5 or 1.5 were less susceptible to high velocity streams near the channel inlet and had lower shear rates too. Another important point of note is that the closer the cell is to the bottom of the trap, the better it is for imaging with the top facing objective owing to the small working distance of high NA objectives. However, this may pose problems related to beam clipping in the bottom facing (trapping) objective.
- Since the Reynolds numbers (ratio of inertial forces to viscous/shear forces) in microfluidic applications are very low, the inertial forces can be neglected and it can

be safely assumed that the viscous shear forces initiate the rotation of the solid body (cell). When steady state is established, with symmetric flow about the rotation axis, the rotational field is a linear function of the angular velocity and the location of the cell inside the vortex (at the center would give best approximation). At steady state, the rotational velocity is approximately the same as the recirculating tangential flow velocity.

- Effects of the microchamber dimensions were investigated and it was shown that the rotation rate was almost the same for an aspect ratio of 2, irrespective of the incident angle. The shear rate (gradient of the velocity vector and indicative of the stability of the microvortex) however, was the maximum and almost the same for every incident angle tested, at an aspect ratio of 1. The shear rate reduced on either side of an aspect ratio of 1; lowest at a ratio of 0.5 for all three angles, but was very different for the three angles (30, 60, and 90) at a ratio of 2.

  In conclusion, trapezoidal features acting as sub-channel micro chambers are effective for peeling off flow because of their sharp undercut edges and easy induction of recirculating profiles thereafter. They also provide easy and distortion-free optical access owing to their flat underside. The microchamber geometry with the least shear rate, strong vortex formation and a high rotation rate would have an aspect ratio of 2 and an incident angle of 30º.

1.5 Summary of contributions

Prior work has already demonstrated the proof of concept of using sub-channel microvortices to allow flow to be detached and enable single live cell rotation. This can be used to obtain functional CT images of the live cell in true 3-D, since cells are spinning about an axis perpendicular to the imaging axis. For the purpose of optimization and characterization, initial efforts were focused on making the microfabrication technique more efficient. The fabrication parameters for the earlier, backside diffuser lithography technique were optimized, so as to make that technique more reliable than before. This method was later replaced by an inclined/tilted exposure technique, so as to achieve the previously set goals of time efficiency, high yield and excellent reproducibility. Details of the new technique and modifications to the old one are discussed in Chapter 2. A PDMS to PDMS demolding technique was implemented to replace the old method of molding PDMS on 170 μm thick cover glass and peeling off from a rigid wafer surface. This new method permitted far greater flexibility in terms of demolding and hence improved the yield to 100%.

A pressure driven pump- flow sensor assembly was procured and set up. This allowed for reliable flow readings with the sensor in the pressure-control mode, while adding a very important dimension with its feedback/flow control mode through the pump-sensor interface. Pilot experiments were performed, to obtain the flow regime required for cell rotation. These experiments also allowed for the determination of optimal trapezoidal chamber inlet widths for cell rotation characterization. The pump-sensor assembly was

calibrated for PBS and water and accurate flow restrictors were added to the microfluidic circuit in order to have the pump working in an optimal pressure range.

Finally, flow rates that would produce various cell rotation rates, for different trapezoidal chamber dimensions at set values of laser trapping power were quantified.

2. MICROFABRICATION MODIFICATIONS AND OPTIMIZATION OF THE CHIP

2.1 Need for optimizing/replacing 3D backside diffuser lithography (BDPL) for trapezoidal feature fabrication

Previous work (Myers 2012) demonstrates proof-of-concept for cell rotation perpendicular about the optical axis using trapezoid microstructures. However, the microfabrication processes using BDPL remain major challenges, in terms of processing time, yield and reproducibility.

- The process took about 12-16 hours (depending on ramp times for baking). Because of the poor adhesion strength between SU-8 2035 and glass substrates, an extra layer of SU-8 2005 on top of a silanization layer was used for promoting adhesion; both of which significantly increased the amount of processing time. Even after using the adhesion promotion protocol, it was observed that a loss of features, hence low yield occurred because an intrinsic limitation of BDPL is that it requires under exposure. Even though KMPR has been demonstrated as having superior adhesion strength to glass substrates compared to SU-8 (Hou et al. 2010), the initial efforts in developing BDPL process using KMPR failed.
- BDPL uses a 180 degree diffuser to scatter collimated light over the exposed area. Therefore, both the sidewalls and the ends have a rounded appearance, which introduces un-swept (dead) volume at both ends. The width of the main flow channel was designed as 3 mm, which was almost the same as the length of the trapezoid trap (2.5mm). The flow pattern inside the main channel and trapezoid with unmatched dimensions was not simulated in COMSOL in previous work. In addition, before the

stabilization of the flow, cells could be trapped inside the un-swept volume and introduce an unpredictable flow pattern.

- High quality imaging requires high numerical aperture (NA) objectives. All high NA (1.1 to 1.4) water or oil immersion objectives available are corrected for a 130-170 µm thick cover glass. Therefore, it is critical to replicate SU-8 or KMPR negative microstructures to a PDMS thin film casted and then cured on a 170 µm thick cover glass. The challenge is to peel off the fragile and rigid PDMS-cover glass (170 µm) assembly from another rigid fused silica wafer (500 µm). The cover glass breaks very easily and the process has to be repeated, resulting in a yield of only about 20-30%.

To summarize, the BDPL process needed to be simplified and optimized to obtain better yield, time efficiency and reliability. This was imperative to be able to produce chips on demand. As a result, it was decided that process parameters for the BDPL technique parameters be optimized for both SU-8 and KMPR to improve its yield. At the same time, the promising method of inclined/tilted lithography was pursued in order to meet the fabrication requirements for trapezoidal features. A series of test patterns were first used to gauge the best parameters for this new process. It was then used to fabricate wafers with trapezoidal features which provide a proof of concept for cell rotation. To address the challenge of peeling off the cover glass from the wafer, a new PDMS-PDMS demolding technique was utilized. Both, the tilted exposure and PDMS-PDMS demolding methods are described in detail, later on in this chapter.

2.2 Optimization of fabrication protocol for backside diffuser lithography

The first step for using backside diffuser photolithography is to transfer a chrome mask pattern to the backside of the wafer itself. The transferred pattern is used as a self-contained mask during exposure. The processes are summarized as follows:

- Coat 4 ″ fused silica wafer with 100 nm Cr (CHA E-beam evaporator or Edwards II thermal evaporator in the Center for Solid State Electronic Research)
- Spin Coat 1 µm AZ 3312 at 3500 rpm for 30 seconds using a precision spin coater (P6700 series, Specialty Coating Systems, Inc.)
    - Soft Bake: 100 ℃, 1 minute
    - Expose: 45 mJ/cm^2 (through a transparency or chrome patterned glass mask)
    - Develop: AZ 300 MIF, 1 min
    - Hard Bake: 110° C, 1 min
- Etch exposed chrome for 1 minute using chrome etchant CR4S, (Transcene Inc.) CR4S containing a mixture of 6% nitric acid and 16% ceric ammonium nitrate in water. min
- Remove AZ 3312 using Microstrip 2001 (Microchem, Inc.) at 65° C-100° C, for 3-5 minutes.

In the original protocol, after an adhesion promotion silanization procedure and another adhesion promotion sacrificial SU-8 layer coating (both explained in detail in table 1), a spin coater was used to spin a 50 µm thick, SU-8 2035 layer onto the wafer. Thereafter, a

soft bake (refer to table 1) was performed to remove all of the residual solvent left in the photoresist after spinning. In the modified protocol, the adhesion promotion steps were replaced by a surface roughening plasma treatment. Thereafter, a 50 µm thick SU-8 3025/KMPR layer was spin coated and soft baked.

Table 1: Detailed process flow of the original protocol and modifications made to it

Important steps	Original backside diffuser protocol	Modifications made
Adhesion promotion silanization procedure	↓ Dehydrate at 160° C for 30 minutes ↓ Oxidize surface by air plasma for 40 seconds at 10 W and 500 mTorr ↓ Immerse for 30 minutes in a 60° C bath containing 300 ml Methanol: 1.5ml 3-(aminopropyl triethoxysilane) (APTES) ↓ Thermal annealing (10 minutes at 160° C)	Not necessary

Adhesion promoting SU-8 sacrificial layer (5 µm)	✚ Spin coat: 6000 rpm for 5 µm thickness ✚ Soft Bake: 1minute at 65° C and then an infinity (>5° C/minute) ramp to 95° C and hold for 2 minutes on a hot plate ✚ Expose: 135 mJ/cm^2 (with and i-line filter, specific to SU-8 and KMPR) ✚ Post Exposure Bake (Ramp at infinity to 95 °C from room temperature [R.T.]) ✚ Hard Bake by ramping from 95° C to 110° C, hold there for 30 minutes before ramping down	Instead of using a silanization protocol or an extra SU-8 layer, a higher power surface plasma treatment process was used (50 sccm Oxygen, 200W, 10 minutes) to provide a rougher surface for promoting SU-8 adhesion

Trapezoid forming SU-8 2035/3025 layer (50 µm)	• Spin coat: 2000 rpm for 50 µm thickness • Soft Bake: Ramp from R.T. to 65° C, hold for 15 minutes; ramp to 95°; remove from hot plate to cool to R.T. • Exposure: 200 mJ/cm^2 • PEB : Ramp to 65° C from R.T. and hold for 60 minutes; Ramp to 95° C and hold for 6 minutes; cool to R.T. • Develop for 10-15 minutes w/o agitation • Hard Bake at 110° C for 60 minutes	• Changed from SU-8 2035 to 3025 and to KMPR 1025, for improved adhesion • Spin coat: 1400 rpm for 50 µm thickness • Soft Bake: Ramp from R.T. to 65 ^{o} c, hold for 3 minutes, ramp up to 95 ^{o} c (100° C for KMPR) and hold for 15 minutes. Ramp down to R.T. All ramps were set to 1°C/minute to minimize the amount of mechanical stress and to promote adhesion. • Exposure: Exposures between 60-90% (i.e. approx. 225-337.5 mJ/ cm^2 for SU-8 and 900-1350mJ/cm^2 for KMPR)

		were tested and all of them worked well - PEB: Ramp to 65 °C from R.T., hold for 1 minute and then ramp up to 95 °C and hold for 5 minutes (100°Cfor 4 minutes for KMPR). Ramp down to R.T. - Develop with agitation for about 8-10 minutes - Hard Bake: 120 °C for 60 minutes at 1°C/minute - Ramp from R.T.; cool to R.T. at 1 /minute to release the stress.

For exposure on an OAI Hybralign series 200 aligner, the wafer was placed face down on another plain glass wafer that was placed on the stage of the instrument by vacuum. From top to bottom, the set-up consisted of the UV light from the OAI aligner, the i-line long pass filter (PL-360LP, Omega Optical), a 5” square opal diffuser (NT02-149, Edmund Optics Co), an index matching layer (IML- water or oil), the face down SU-8/KMPR

coated fused silica wafer and a plain support wafer held on the instrument stage by vacuum.). The diffuser and filter setup was on a separate mask holding module of the instrument (as shown in **Figure 1-top**), which had to be brought into contact with the rest of the setup by moving the stage up (**Figure 1-bottom**). This facilitated even distribution of the IML over the surface of the wafer and uniform diffusion of light.

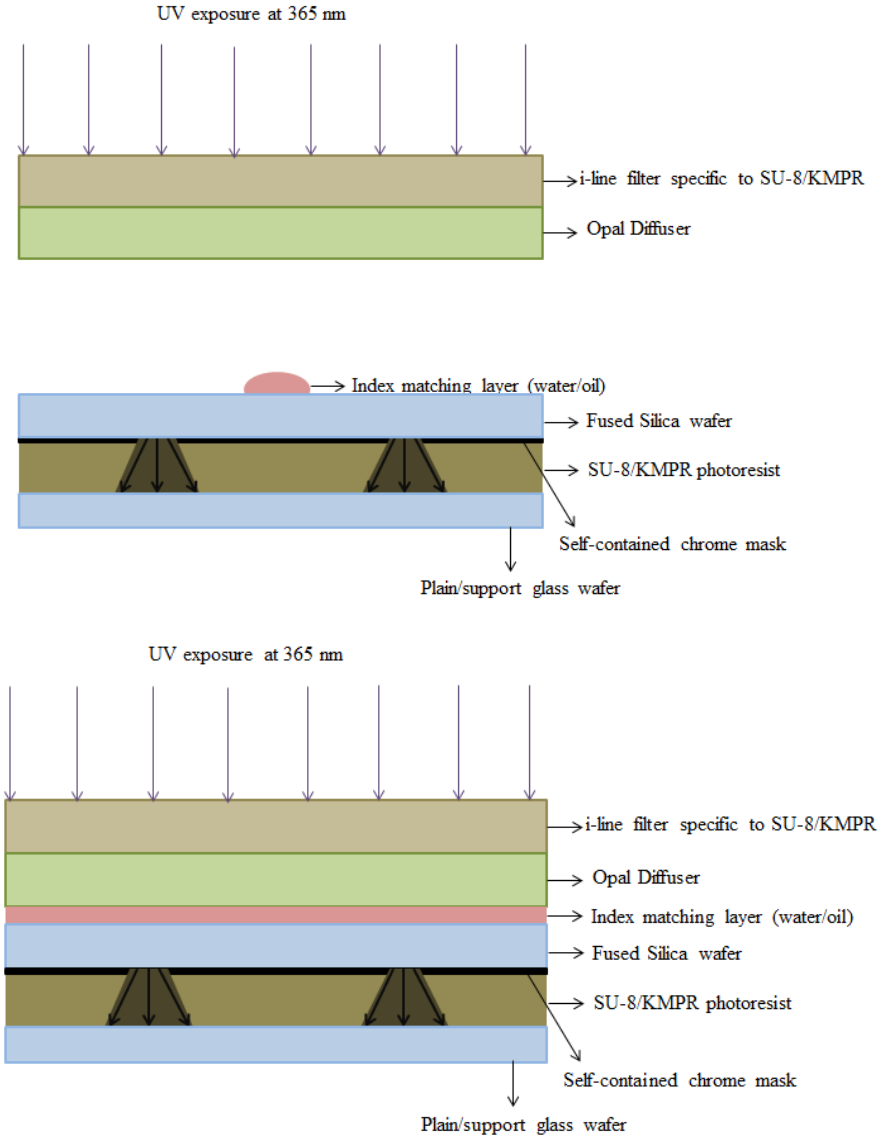

Figure 1: Schematic of backside diffuser photolithography before (top) and after (bottom) moving the stage up

Following the post exposure baking process (refer to table 1), the SU-8 photoresist is developed for either 15 minutes, without agitation (as in the original protocol) or for 8-10 minutes with agitation (as in the modified protocol) in SU-8 developer (1-Methoxy-2-propanol acetate, Microchem Corp), washed with isopropanol, and dried with N2 gas. Similarly, the KMPR photoresist can be developed using the same SU-8 developer for 3-5 minutes or using a TMAH (0.26 N) aqueous alkaline developer (Microposit MF26A, Shipley Europe Ltd.). Finally, the wafer is hard baked (refer to table 1) at 160 °C to further crosslink SU-8/KMPR and enhance the adhesion. Cross-section of PDMS replicates from SU-8 and KMPR trapezoid microstructures are shown in Figure 2.

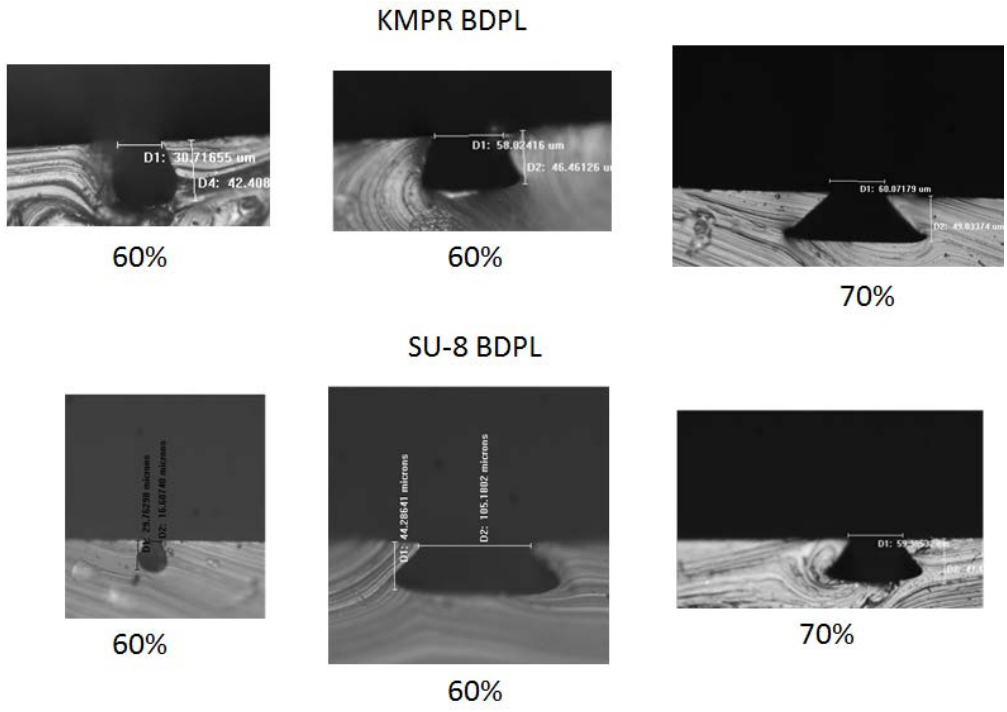

Figure 2: KMPR and SU-8 cross-sectional features after use of BDPL technique

As can be seen from Figure 2, the bottoms of the trapezoids are not flat, especially for trapezoids with narrower necks. It is attributed to the lower dose of UV light through the narrower transparent area on the self-contained chrome mask. Even for the widest neck of 105 µm, the roundness of the bottom is still discernible. Although the optimized process gives a 100% yield, this BDPL process is still time consuming and the unswept volume at both ends of trapezoids in addition to the rounded bottoms are the intrinsic limitations.

To address these issues posed by the BDPL technique, we developed a simple and effective backside tilted UV exposure method as detailed in the next section.

2.3 Tilted backside UV lithography

Owing to its flexibility in terms of the feature angles that can be achieved with the use of a tilted angle of exposure, the method of inclined UV lithography has been gaining a lot of ground in recent years. This method is based on the principle of light refraction. Once the indices of refraction for the media in the setup are known and the required angle of tilt on the final features is determined, a specific angular block can be used to provide the correct incident angle, based on calculations. The formula used for this comes from Snell's law: $n_1 \sin\theta_1 = n_2 \sin\theta_2$; where n_1 is the refractive index of the first medium, n_2 is that of the second medium, $\sin\theta_1$ is the angle of incidence and $\sin\theta_2$ is the angle of refraction. The angle to confirm would give results with cell rotation the same that was achievable with the backside diffuser method, i.e. 56º (as with water as the IML). The angle achievable with oil is 46º, but to achieve that angle on the inclined exposure

method would require exposing the wafer inside a glycerol bath to allow for good index matching and minimal refraction. However, with the decision to fabricate features that would give identical angles as on the backside diffuser, it was determined that a 60º block would achieve an angle of 57.7 º with KMPR and 58.34 º with SU-8. This can be calculated using Snell's law given that air, which is the medium of incidence, has a refractive index of 1.00; the second medium of interaction is fused silica glass (wafer substrate) which has a refractive index of 1.4745 at 365 nm and the final medium is the photoresist, SU-8/KMPR with an index of 1.65 for SU-8 and 1.62 for KMPR (at 365 nm, from the Microchem datasheet). The chrome layer is not considered here since the area where the photoresist (PR) is exposed does not contain any chrome and hence the light passes directly from the glass into the PR layer. The UV light comes in at an angle of 90 º to the xy-plane and hence, by tilting the wafer to 60 º, the incident angle of the light is at 60 º with respect to the normal to the surface of the wafer. The minimum achievable angles with KMPR and SU-8 are 52 º and 52.8 º respectively. However, by dipping the whole setup into an index matching liquid like glycerol, this minimum can be extended down to 19 º (Hung, Hu, and Tseng 2004). A schematic of the tilted exposure setup is shown in **Figure 3**. Assume in this figure that the wafer (tilted on a 60º angle is now on the horizontal plane at 0 º, so that the incident ray of light makes an angle of 60 º with a line perpendicular to the point of incidence.

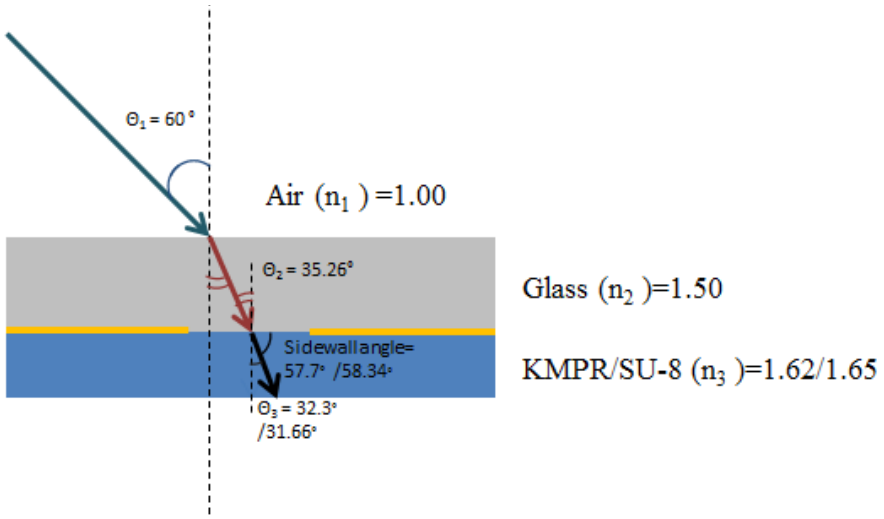

Figure 3: Schematic of how a 57º sidewall angle can be obtained using a 60º block to incline the wafer

The setup for the tilted exposure is shown in **Figure 4**. As can be seen, the UV light passes first through the i-line filter (balanced on two blocks to keep it horizontal) and then passes through the glass wafer. Finally, it is incident upon the KMPR/ SU-8 photoresist layer. A test pattern of nine replicas of the pattern (widths ranging from 20-150 µm) as shown in **Figure 5**, was drawn on AutoCAD (Autodesk Inc.) on a 5" square mask and then transferred to the wafer (to make it a self-contained mask) using the procedure outlined in Section 2.1. This wafer was diced into nine different chips (each containing the test pattern shown in Figure 5). Following this, the chips were plasma treated using 200 W, 50 sccm oxygen for 10 minutes. Each chip was then spin coated with KMPR 1025/SU-8 3025, soft baked and mounted, photoresist side facing down, to the 60° inclined block. Different chips were subjected to different exposure doses ranging from 60% to 100% of the full exposure doses for SU-8 (375 mJ/ cm^2) and KMPR (1500

mJ/ cm^2), both of those exposure doses were determined after considering the fact that a glass substrate needed 1.5X the exposure dose, as mentioned in the Microchem datasheet. For exposure, as seen in the schematic in **Figure 6,** the chip is first exposed at 60° to form the first half of the trapezoid and then turned 180° and exposed again to expose the second half. In case there is un-exposed area because of the narrow open window, a third backside flood exposure without any inclination was performed. After exposure, the chips were post-exposure baked, developed and hard baked as explained in Table 1 (modifications column). Cross sections of the PDMS mold replicated from a few of these chips are shown in **Figure 7**. In addition, the angle measurements for SU-8 and KMPR are shown in these images match the values obtained from theoretical calculations.

To modulate sidewall angles and observe how this affects the stability of the microvortex itself, the 60° inclined block used for backside tilted exposure as explained earlier, was modified slightly. This involved immersing the wafer taped to the block in a water bath (NA=1.33) to achieve a closer index matching to the glass wafer than air (NA=1.00). This allowed reduction of the angle of incidence according to calculations to approximately 45° for KMPR 1025. After testing various exposure doses on chips with the pattern shown in Figure 5, a 100% yield was achieved with exposures ranging from 60-80% of full exposure for KMPR 1025. Some of the features obtained are shown in **Figure 8**.

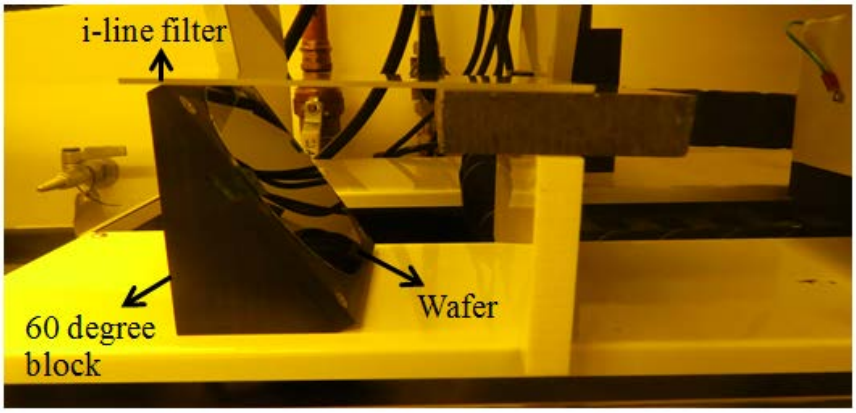

Figure 4: Setup for tilted exposure on the OAI stage

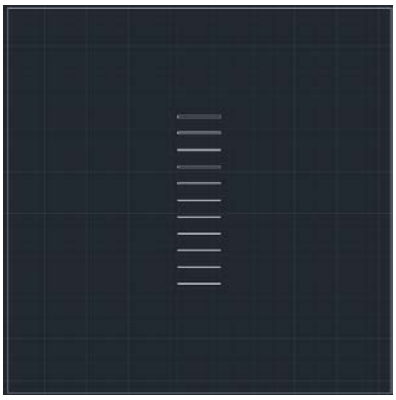

Figure 5: From bottom to top, test pattern with opening widths of 20-150 µm. Nine such patterns/chips were obtained from one wafer

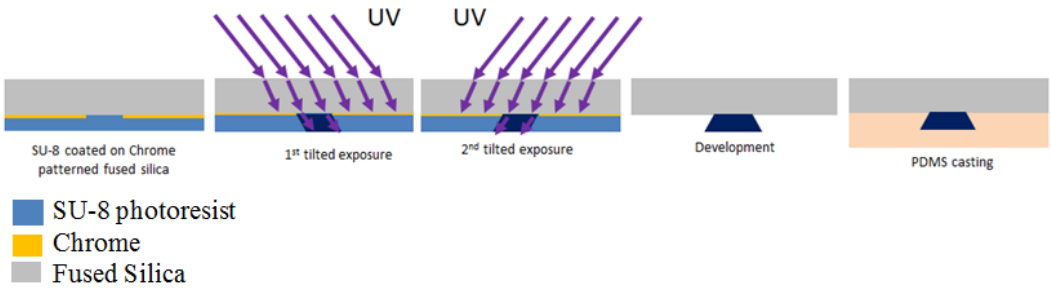

Figure 6: Schematic of tilted/inclined exposure, development and finally, PDMS casting for mold making

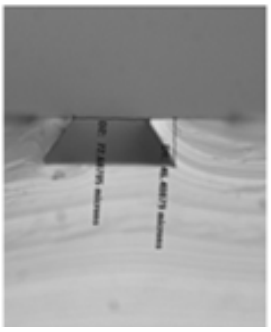

90% tilted KMPR

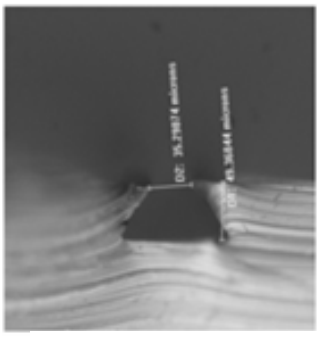

80% tilted KMPR

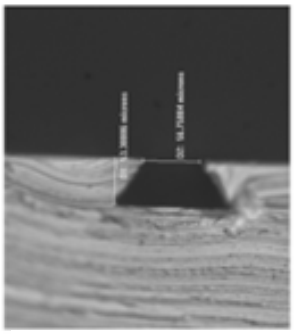

60% tilted SU-8

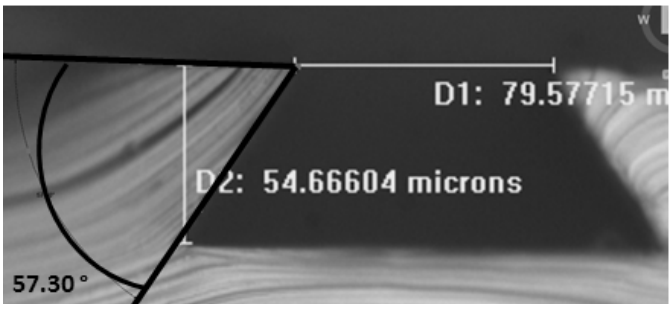

57.30° (57.7º, theoretically) sidewall angle obtained on KMPR

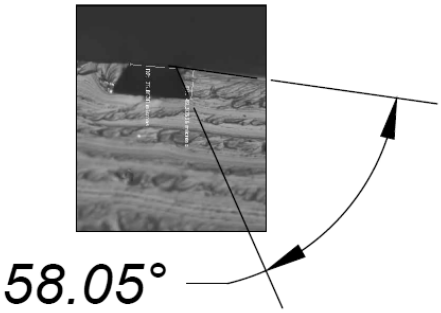

58.05° (58.34º, theoretically) sidewall angle obtained on SU-8

Figure 7: Different tilted exposure doses on SU-8 and KMPR and the angles (calculated on AutoCAD) obtained on the sidewalls

Comparisons between the tilted exposure and the backside diffuser lithography features on a non-contact 3-D profilometer (Figure 9) revealed that the ends of the trapezoids while being rounded (reason for unswept volume), were more flat on the tilted exposure features. This meant that the dead/unswept volume was minimized by taking out the diffuser component which spread light in all directions at the same angle.

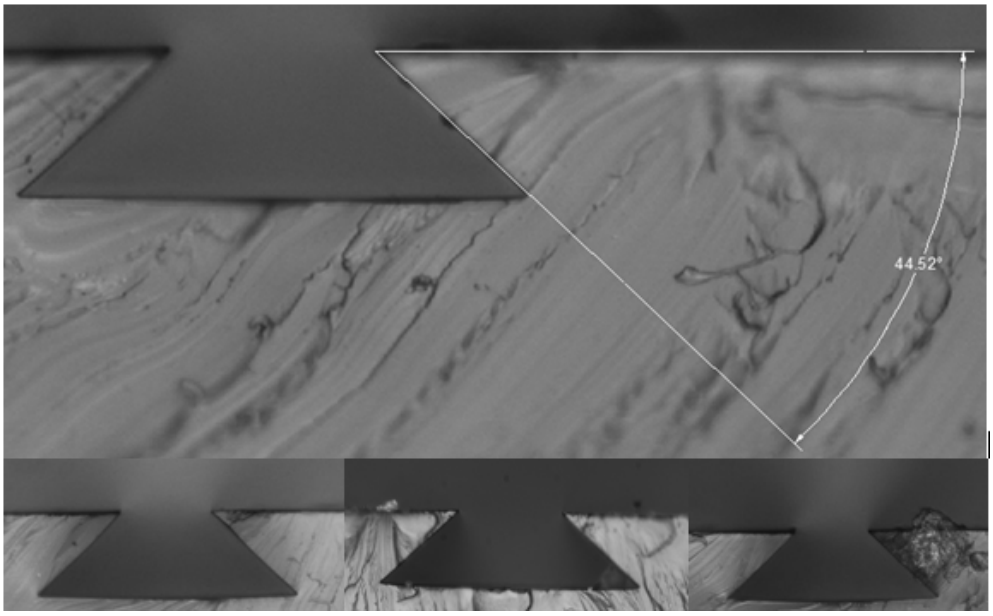

Figure 8: **Sidewall angle modulation (~ 45°) using water bath immersion during exposure**

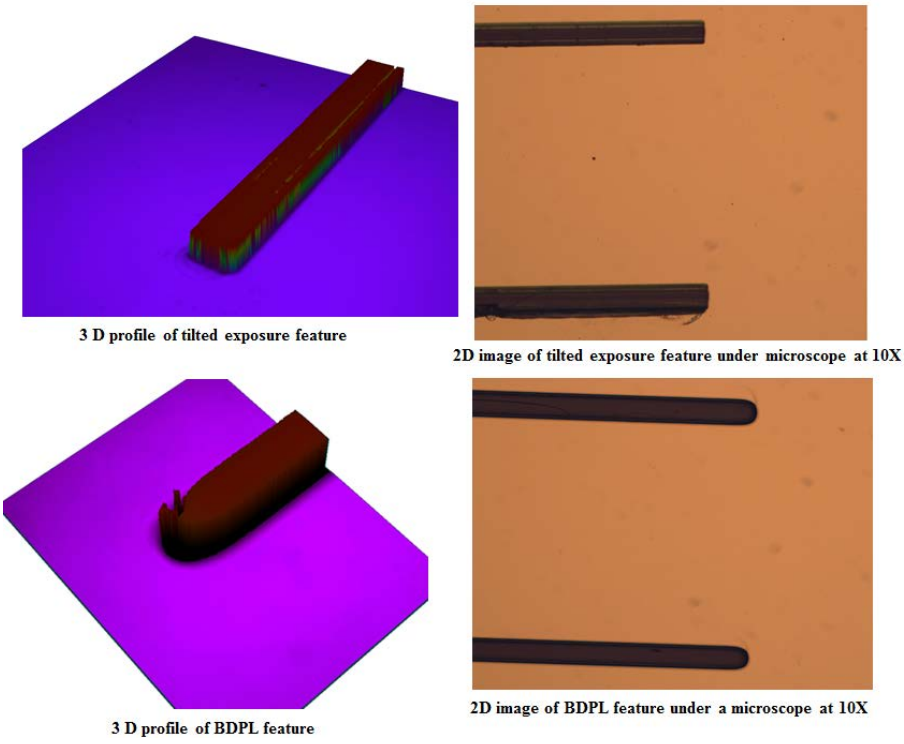

Figure 9: 3D and 2D profiles for tilted exposure and BDPL features

As a result of this reduction of unswept volume, it is easier to make the features as small as needed, lengthwise.

The improvements that have been made with the tilted exposure technique are summarized as follows:

- The processing time was reduced almost by 50% (compared to the original protocol described in Table 1) since there was no need for any adhesion promotion protocols. The bake times and ramps (1°C/min) were well defined and as a result, there was good control on process parameters at every step. The yield was improved to 100% when whole wafers were fabricated; i.e. every feature was retained. The process was also easy to reproduce.
- Sidewalls angles from the BDPL features could be easily replicated by using the particular tilted angle, down to 52 º for KMPR and 52.8 ° for SU-8. If needed, by immersing the setup into glycerol, which has the ability to form sidewall angles of down to 19º. The tilted backside exposure is more robust in tuning sidewall angle, compared to BDPL, which is restricted by the availability of IML with required refractive index. The bottoms of the trapezoids were flat, which provided for interference-free imaging, as compared to the round-backed trapezoidal features obtained from the BDPL technique.
- Because of their inability to produce flat bottomed features at smaller opening trap widths, these particular features could not be used while imaging cell rotation. As a result, if data for different aspect ratios and their effects on cell rotation needed to be

obtained, the thickness of the photoresist layer itself would have to be changed to address this challenge. In comparison, with the tilted exposure technique, cells could just be switched to another trapezoidal feature to accomplish a change in aspect ratio (without having to fabricate another chip). Both ends of the features were flat with the tilted exposure, compared to round with BDPL, which meant that the unswept volume was minimized and the lengths of the traps could be made smaller without too much interference with the flow profile.

2.4 Soft lithography of wafer features and improvements made through the PDMS-PDMS demolding technique

After the hard bake was done, the features were ready to be replicated onto PDMS in a non-conventional soft lithography process, while being bonded to a 75 mm x 50 mm piece of 170 μm thick microscope cover glass (Ted Pella Inc.); needed for high quality imaging. PDMS will stick to most glass surfaces, unless they are pretreated with an anti-adhesion silane, and that is exactly what was needed to make the process of delamination easier. The wafer with the features was first oxidized with air plasma for 45 seconds at 500 mTorr and 10 W. Tridecafluoro-1,1,2,2-tetrahydrooctyl trichlorosilane was vapor deposited onto the wafer surface in a desiccator, by applying vacuum for 45 minutes-1 hour. Following this, a 10:1 ratio of PDMS-to-crosslinker was thoroughly mixed, poured into a dish and degassed (in a desiccation chamber under vacuum) until all the bubbles were removed. A few times, a higher, 15:1 ratio of PDMS to crosslinker was used to promote more even spreading after casting. Thereafter, a cover glass was oxidized and

activated with air plasma (500 mTorr, 10W, 50 seconds). A bare minimum amount of PDMS, enough to cover the surface area of the features was then poured onto the wafer and the cover glass was placed over the PDMS so that it would bond to the PDMS while the PDMS was cured in an oven at 60 ºc for about two hours. Nearly 500 grams of weight was set on top of the glass to ensure uniform spreading of the PDMS (as soon as it was placed in the oven) and also to minimize the PDMS layer thickness so that it would match almost perfectly with the thickness of the mold. After it was completely cured, the PDMS mold, now adhered firmly to the cover glass was peeled off from the wafer.

For the flow channel portion of the chip, a similar replication procedure was applied. However, instead of making the mold on the rigid fused silica wafer, a method was adapted (Luo et al. 2007), using a laser (Universal Laser Systems XL-9200) to cut 100 μm thick pieces of Melinex (Fralock Materials) with adhesive on 2 sides, in the shape of channels. These pieces were then adhered to a 250 μm thick polyester film (10 mil Melinex, Fralock Materials). A10:1 ratio of PDMS to crosslinker was degassed and poured onto the mold and a cover glass was oxidized and placed on the PDMS. Weight was applied and after curing at 60 ºC, the cover glass with the PDMS channel mold was taken off the flexible Melinex mold. Two 350 μm diameter inlet and outlet ports were then cut out with a high-powered 355 nm laser using a PotoMAC laser ablation system. The two halves were then oxidized/activated using air plasma for 1 minute at 500 mTorr and 10 W (to form siloxy groups) and were bonded together, making sure that no air gaps were present between the two halves (which would cause leaks when flow was initiated).

It was also ensured that the channel and trapezoids were correctly aligned. Immediately after contact, the device was annealed for 20 minutes at 60 °C. Finally, nanoports (Upchurch Scientific) were attached as inlet and outlet. The multilayer assembly is depicted in **Figure 9**.

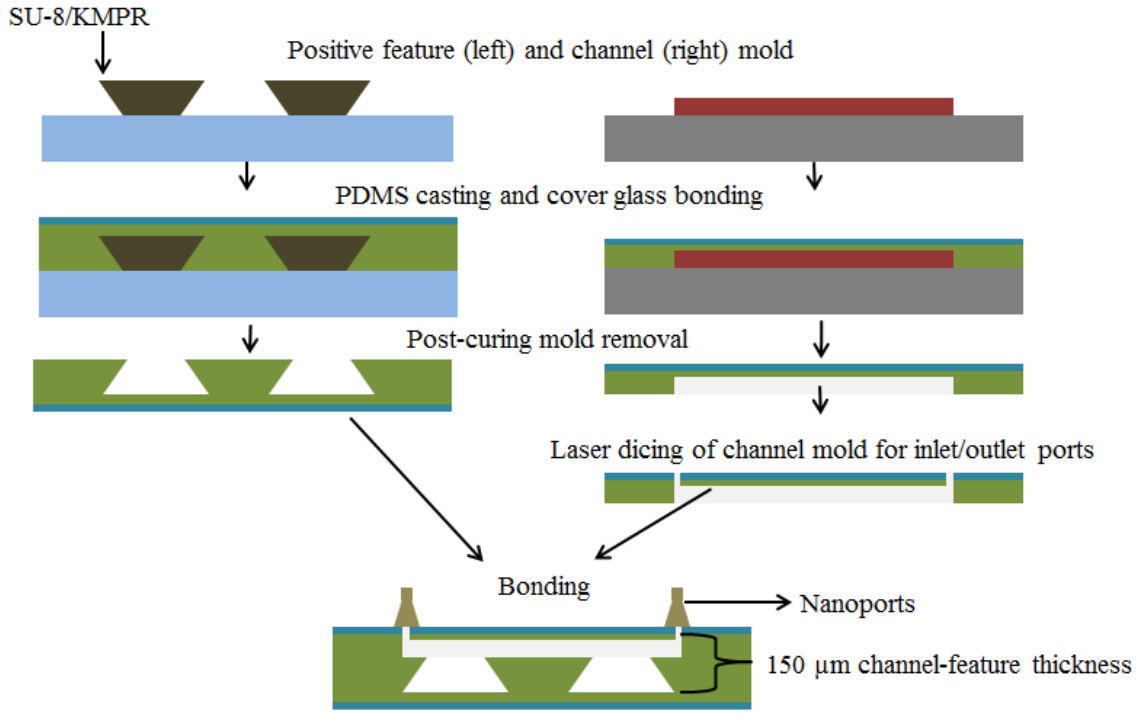

Figure 10: Schematic of multilayer assembly process to obtain the final chip

The problem with this setup was that both the wafer (mold) and the cover glass were rigid materials. The cover glass needed to be 170 µm thick for high quality imaging and as a result, it would break during the demolding process resulting in a yield of only 20-40%.

To overcome this problem, a PDMS-PDMS demolding technique (Shao et al. 2012) was applied to allow for the final cover glass bonded PDMS mold to be peeled off from a

flexible PDMS (positive) mold instead of the rigid glass wafer which was previously used. A schematic presentation of this method is shown in **Figure 11.**

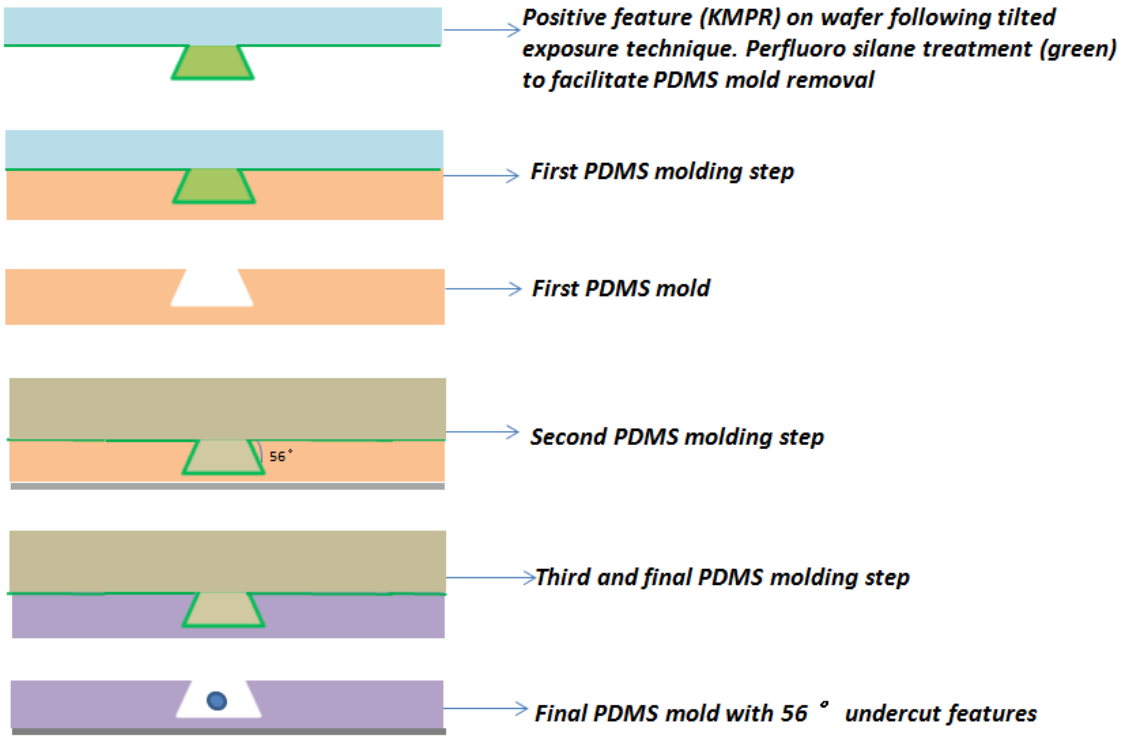

Figure 11: Schematic of the PDMS to PDMS demolding technique showing the three molding steps required to obtain the final mold bonded to cover glass

Although this method does take longer because of the two extra molding steps, it is much more reliable and gives a 100% yield as opposed to the 20-40% yield from the previous setup. As can be seen from **Figure 12,** the replication process for the three molds is seamless and each one of them is an almost exact (albeit opposite) replica of the previous mold. Each of the molds is silanized prior to molding to allow for easy demolding.

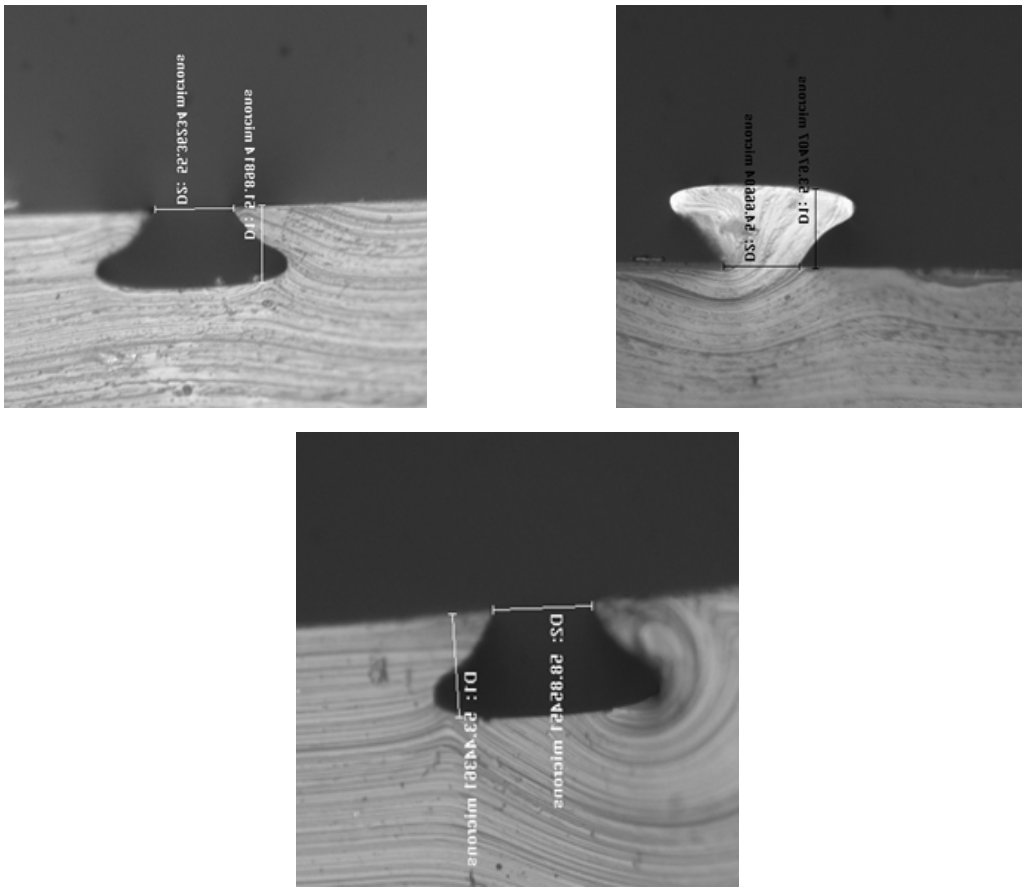

Figure 12: Proof of concept on the working of PDMS to PDMS demolding. Cross sections of PDMS molds on each step of molding and demolding

2.5 Discussion and application of some other techniques

The tilted exposure technique and the PDMS-PDMS demolding techniques have been discussed in this chapter. Their advantages over previously used methods have also been outlined. Some other techniques that were employed, but were not as successful for soft lithography as PDMS-PDMS demolding are described here.

Before the PDMS-PDMS demolding technique was successfully implemented, o flexible layers were used to peel off the wafer surface. . These layers had to depend on chemically manipulating the material of interest so that it would stick to PDMS. The material also had to have a fairly close resemblance to the optical properties of cover glass and comparable thickness, to be compatible with high quality imaging. One such material was a cyclo olefin polymer (COP) called ZeonorFilm (Zeon chemicals L.P.), specifically the 188 µm thick, 1.53 refractive index type of film, ZF 14-188 (or ZF 16-188). A schematic of how this method was expected to work to replace cover glass can be seen in **Figure 13**. Two techniques of doing this were explored; one outlined by Aran et al. 2010 and another one proposed by B. Cortese et al. 2011.

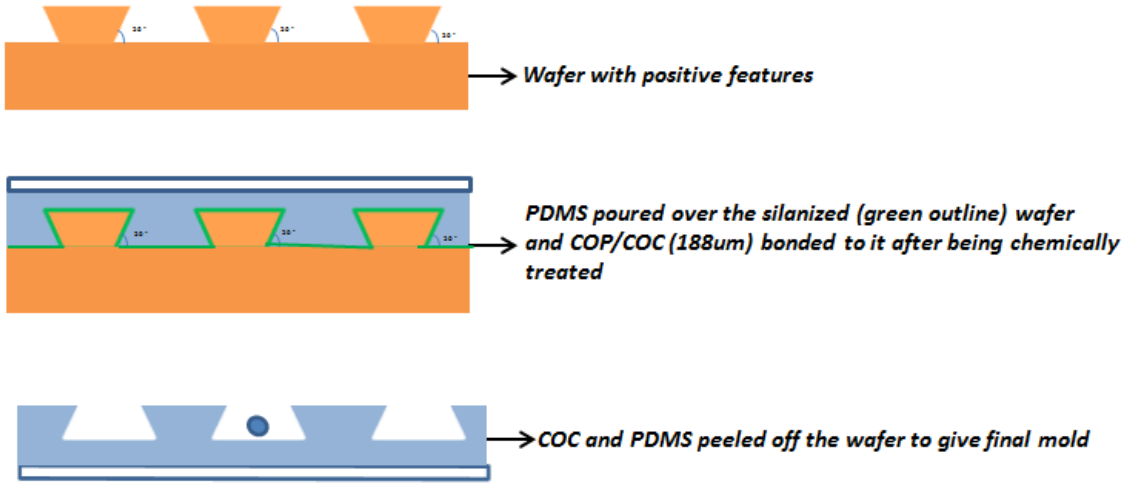

Figure 13: Schematic of COP/COC-PDMS bonding and mold formation

The former technique used 3-aminopropyltriethoxysilane (APTES) as a chemical crosslinking agent to silanize the polymer layer which would help bond PDMS and polymer membranes together. The latter technique used APTES and 3

glycidoxypropyltrimethoxysilane (GPTMS) to treat COC and PDMS respectively, after which the two layers were bonded together. However, both of these methods failed to work as well as the PDMS-PDMS demolding technique in terms of adhesion between the polymer and PDMS layers. The second technique was thought to be a more promising one because of the use of an epoxy based (GPTMS) silane in conjugation with the amine-based (APTES) silane allowing the APTES to act as the linkage with the epoxy groups provided by the GPTMS, forming a strong oxygen-hydrogen bond. However, the GPTMS had a reaction with the water or the solvent during the silanization of the PDMS, leading to a white, sticky residue which stuck to the vessel as well as the PDMS and the bond between the COC and PDMS was not strong enough to be usable. An EDC-NHS treatment of the COC (which would promote bonding between the carboxyl group of the COC and the APTES treated amine-groups of the PDMS surface) also failed to produce a satisfactory bond with the PDMS layer. So overall, the PDMS-PDMS demolding technique seemed to be the best way to go in terms of optimizing the soft lithography part of the process.

Based on pilot experiments conducted on cell rotation, as will be explained in Chapters 3 and 4, the channel molds were also made on a wafer instead of a Melinex sheet. This allowed the channel height to be reduced to 50 μm instead of 100 μm with the Melinex. This was done using conventional front-side lithography of KMPR/SU-8 on silicon wafers; consequently contributing to the larger objective of moving in the direction of working with single cells in the entire chip.

3. SYSTEMS INTEGRATION, PROOF OF CONCEPT AND PRELIMINARY RESULTS ON CELL ROTATION USING NEW PUMP AND SENSOR SETUP

3.1 Flow sensor and pump

The sensor (SLG1430-025, Sensirion Inc.) used previously (Myers 2012) only had a 25 μm inner diameter; as a result of which, there were frequent clogs. This led to an inability to get any flow through the sensor to deliver to the microfluidic chip. The pump assembly had two electro-pneumatic pressure control regulators which controlled positive and negative pressure, based on the voltage that was supplied to them. A 6-port, 2-way valve (MXP7900-000, IDEX Inc.) was used for sample loading and then delivery. A LabVIEW program provided user interface to the pump so as to record the flow rate from the meter, control the valve positions, and control the pressure regulating voltages. The information was saved into a spreadsheet allowing accurate measurements of the component values versus time. Debugging the setup was very time consuming and hence the need was to have the whole system well packaged in a single compact unit, so as to avoid connection problems from constant handling.

A flow sensor was needed with a large enough inner diameter to avoid clogging, but at the same time had extremely good sensitivity and a short response time. Dolomite Microfluidics manufactured an array of flow sensors which could also be integrated with various microfluidic pressure pumps. The different sensors were investigated and based on empirical data, it was determined that the range of flow needed would be in the few thousands of nL/min range. As a result, a sensor which could measure flow ranges from

0.4-7 µL/min was procured (Mitos flow sensor, 320099). This sensor had a flow rate accuracy of 10%, a response time of 30 ms, could handle a maximum pressure of 100 bar (approximately 1440 psi), had a maximum pressure drop of 5 mbar across it, and most importantly, it had an inner diameter of 150 µm. This would ensure that if the liquid was adequately filtered, there would be no clogs in the sensor, ensuring uninterrupted flow to the microfluidic chip. A picture of the flow sensor is shown in **Figure 14.**

Figure 14: Dolomite microfluidic flow sensor (Part no. 320099) with a measuring range of 0.4-7 µL/min

A microfluidic pump (Mitos p-pump basic, part no. 3200175) was also acquired from Dolomite, so that it could be tested in conjugation with the flow sensor. This pump provides pulseless liquid flow with a precise pressure driven pumping mechanism and operates over a pressure range of 0-10 bar (0-144 psi, approximately). A picture of the basic p-pump can be found in **Figure 15.**

In general, the level of pulsation in a system is determined by the system elasticity. Low elasticity is characteristically rigid in terms of tubing and the microfluidic device and results in a high degree of pulsation. High elasticity systems are generally characterized by elastic tubing, elastic microfluidic device and the presence of gas bubbles and act to damp out much of the pulsation. The p-pump has a flow smoothness of ± 0.1% and a response and settling time of < 4 seconds for pressure changes/steps of over 5 bars (< 3 s for a 1 bar step); over both types of system elasticity.

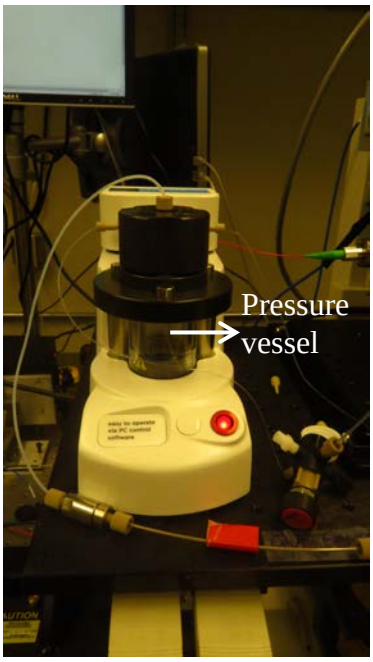

Figure 15: Microfluidic pump (p-pump basic, Dolomite microfluidics) with connections for delivery to the microfluidic chip

The p-pump, through integration of the flow sensor, can provide flow control in addition to pressure control, which makes experiments easier to set-up and optimize. With the

Mitos flow rate sensor connected in-line between the pump and the microfluidic device, a target flow rate of interest can be set on the p-pump software and the pump pressure will automatically be adjusted to meet the target flow rate. A schematic of the working of the p-pump is shown in **Figure 16** and **Figure 17** shows the presence of an in-line flow sensor, integrated with the pump for closed-loop flow control. Some of the other important features of the pump are a pressure resolution of 0.001 bar (0.01 psi), a pressure stability of 0.1 % of the system pressure (minimum of ± 0.002 bar), a weight of only 2 kg, and it can accept fluid volumes from 100 µl to 30 ml in vials/vessels in the pressure chamber.

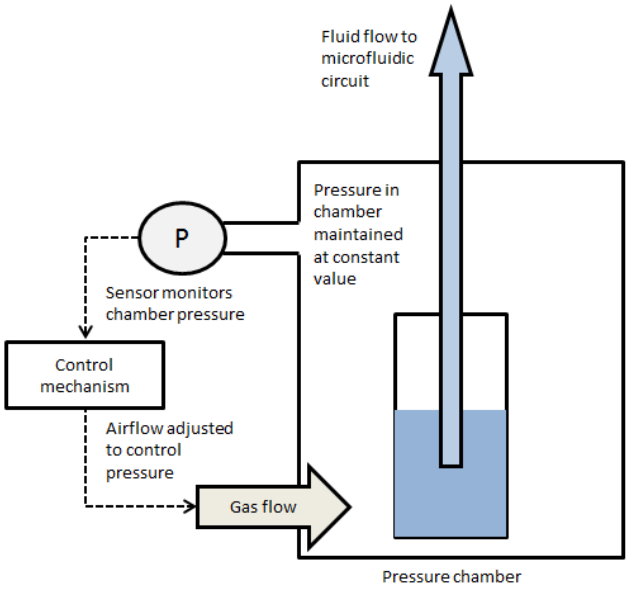

Figure 16: Mechanism of flow/pressure control in pressure chamber in the p-pump

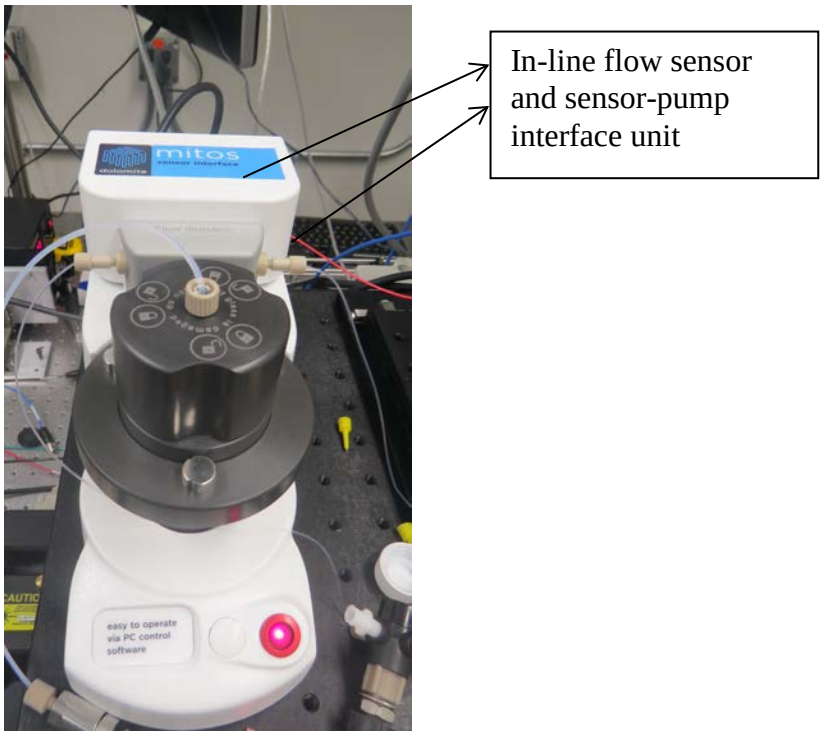

Figure 17: In-line flow sensor with the Mitos sensor interface which allows for sensor-pump integration and consequently, closed-loop control

The performance of the sensor is based on a CMOSens technology (Sensirion, Westlake Village, California). This technology combines a high precision sensor element with amplification, A/D conversion and digital signal processing on one single CMOS chip. It uses a thermal flow measurement principle wherein a heating element on the microchip adds a minimal amount of heat to the medium. Two temperature sensors symmetrically positioned above and below the heating element detect the slightest of temperature differences. Since spread of heat is directly related to the flow rate, these temperature differences can be directly converted to flow rate measurements by the sensor. The flow sensor is primarily calibrated for water, mineral oil and certain other fluids; however, to

have the cells introduced in a cell-friendly environment, the fluid of choice was Dulbecco's Phosphate-Buffered Saline (DPBS, Sigma Aldrich). As a result, it was important to make sure that the system was calibrated for DPBS, so that it was known how much different the flow rate was for DPBS than it was for water, while having the software run in the water calibrated mode, since water has the closest density to DPBS. The density of DPBS was first calculated using the Density= Weight/ Volume formula to be 1.021 mg/µL as opposed to 1mg/µL for water. Two separate vessels, one containing DI water and the other containing DPBS, were used as inlet vessels in the p-pump's pressure chamber and two empty collection vials were weighed prior to starting flow. Flow rates of 10, 20, 30, 40 and 50 µL/min, using a new flow sensor which worked in the range of 1-50 µL/min were set for 15 minutes, each. After the respective liquids had been collected at each flow rate, the weights of the collecting vessel were measured, and were compared to the initial weight before flow was initiated. Once the weight had been measured for each step for the respective liquids, using the relationship Flow rate= weight/time, given the time for which the liquids were collected at each flow rate, density of the liquids and the weights of the collecting vessels, the actual flow rates were calculated. A graph of the calibrated flow rate curves for water and DPBS for the set flow rates is depicted in **Figure 18**. **Table 2** shows the values obtained for these tests for the five preset values on the software.

Table 2: Calibrated values for water and DPBS at the five different set flow rates

Input values (µL/min)	Measured flow values- DI Water (µL/min)	Measured flow values- DPBS (µL/min)
10	9.85	9.9315
20	19.84	20.1715
30	30.15	30.258
40	40.64	40.619
50	50.85	50.13

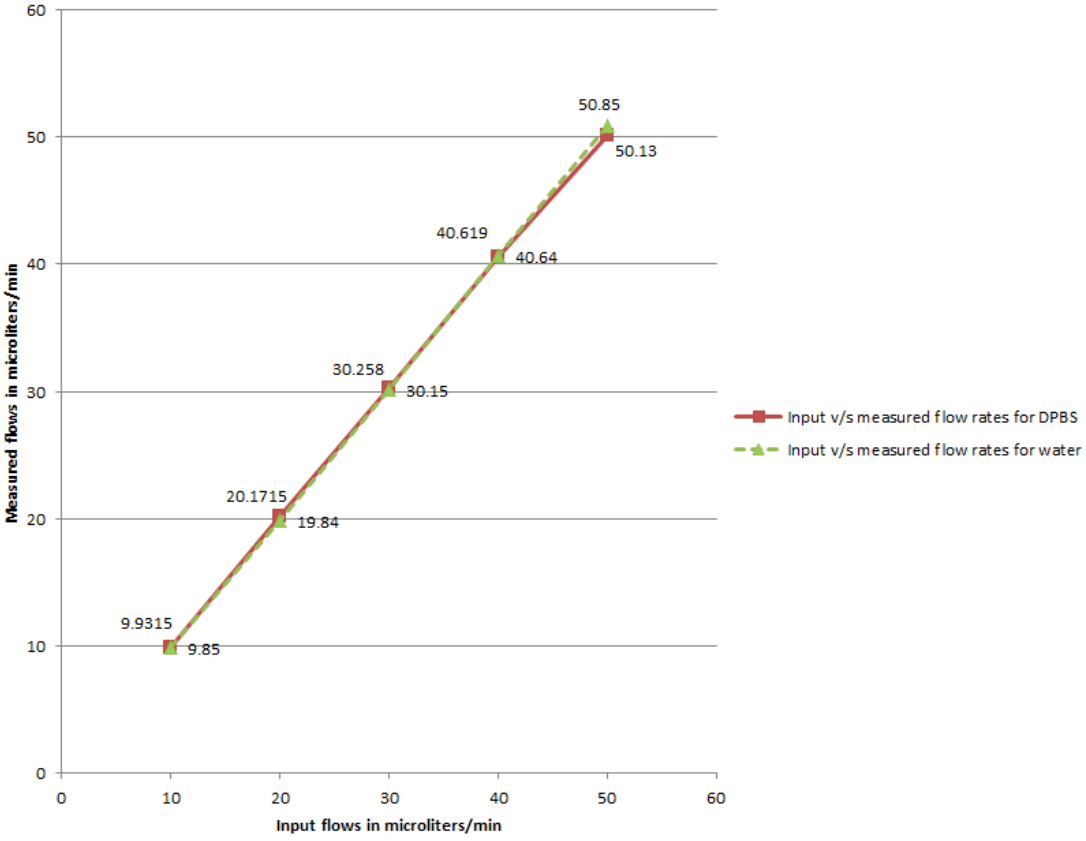

Figure 18: Calibration curves for water and DPBS at five different set flow rates

As can be seen from **Figure 18** and **Table 2**, the responses for both fluids are almost linear and the flow rates of DPBS are only 0.0085% different from those of water, i.e. it can be safely assumed that the flow rates set on the software with water as the calibrated fluid can be used for DPBS as well, without having to compensate for the change in density or other properties of DPBS. The only thing that needs to be done to ensure that no salt deposits are formed on the sensor is to flush the system with water (after using DPBS) and blow air through the sensor. A screenshot of the computer software interface with the pump and sensor assembly is depicted in **Figure 19**. As can be seen from Figure 19 the software provides graphs of the pressure and flow rates, which are also recorded in the form of Excel spreadsheets (data logs). There are also options on the software to tare the pump and/or sensor in addition to provision for a leak test to make sure the pump is working optimally.

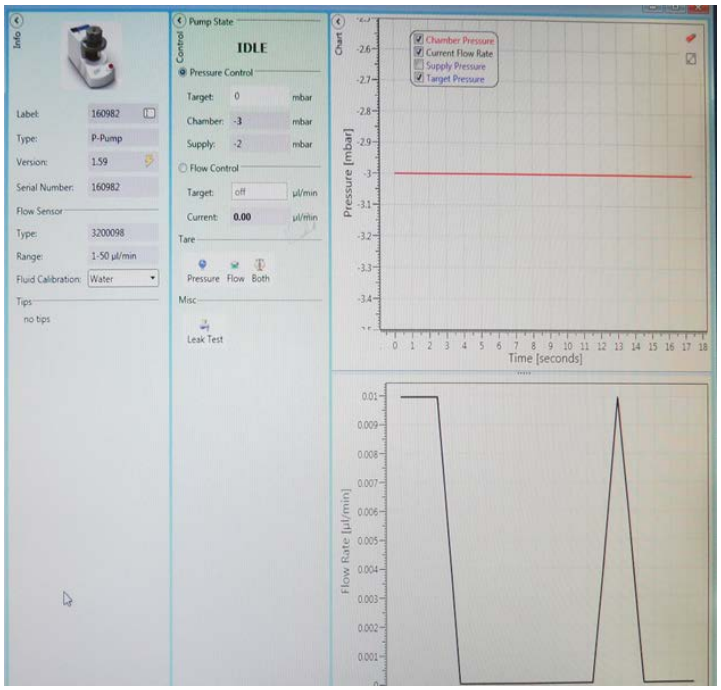

Figure 19: **Dolomite flow center software for interface with the sensor and pump**

3.2 Optical tweezers and imaging setup for trapping and manipulation of cells in the vortex

To accomplish micromanipulation of cells and beads, an optical tweezers setup was used as can be seen in Figure20. A 1064 nm, 600mW diode laser (LD-1064-BF-600, Innolume GmbH) was coupled through a single mode fiber to a beam expander. This produced a 12 mm collimated beam to roughly match the objective back aperture. The beam was then reflected off an 825 nm short pass dichroic mirror (Omega Optical Inc., Brattleboro, Vermont) and focused through a plan-apochromatic (corrected for both spherical and chromatic aberrations)60X (NA=1.2) water immersion, objective lens.. The objective focused the laser beam to form a strong optical trap, provided that the beam had an almost Gaussian profile and was accurately aligned so as to not be clipped by the objective. . White light from an LED source was focused through an apochromatic (corrected for chromatic aberrations) 40X (NA=1.15) water immersion objective, mounted on an inverted Nikon TI-S microscope. A joystick was used for moving in the xy-plane. Z-axis control was established through the use of a spring-loaded mechanism allowing for micrometer range precision control. The light transmitted through the specimen was collected by a CMOS camera (DCC 1545C, Thorlabs), mounted on the (trapping) objective. A CCD camera, the Prosilica GE 1650 (Gigabit Ethernet type, Allied Vision Technologies, Newburyport, Massachusetts) was mounted on the right bottom port of the microscope and used for bright-field imaging. The left bottom port was coupled to a swept field confocal (SFC) scanner unit conjugated to a sensitive CCD camera, the QuantEM (with electron-multiplying gain, Photometrics, Tucson, Arizona).

This camera was used for both, unstained and fluorescently labeled live or fixed cell imaging. The SFC unit (and a laser launch, both from Prairie Technologies, Middleton, Wisconsin) was driven by a combination galvanometer and piezoelectric crystal scanning setup for z-axis optical sectioning. This system allowed high quality confocal fluorescence imaging to be accomplished. It could provide 100 fps in pinhole imaging mode and 1000 fps in slit mode. The piezo could execute high-speed z-stack acquisitions with a travel range of ~150 µm and 0.1 µm step size. The Prairie View software enabled collection of z-series and t-series images. The optical trapping system and the imaging components can be seen in **Figure 20**.

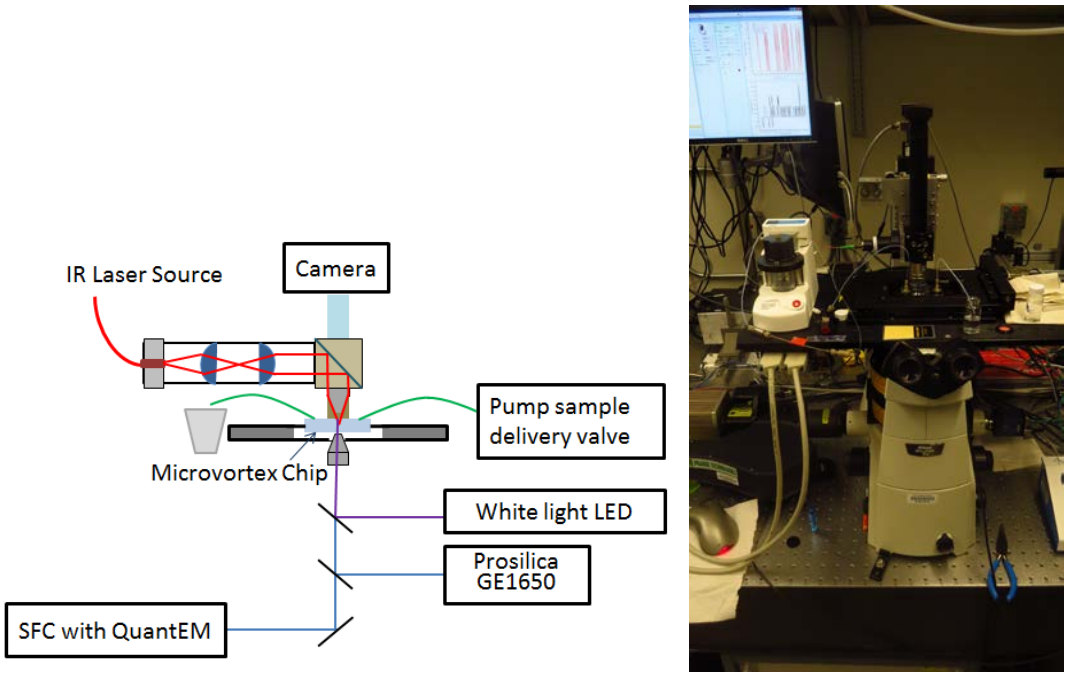

Figure 20: Schematic of optical trapping and imaging setup (left) and experimental setup (right)

4. CHARACTERIZATION DATA

4.1 Preliminary cell rotation data

Live K562 (human immortalized myelogenous leukemia) cells were rotated inside the microvortex about an axis perpendicular to the imaging axis. The important objective was to demonstrate the ability to rotate live cells using the new pump and sensor setup, while also trying to gauge the flow rate regime to get cells to spin regularly and in a fairly stable manner.

As can be seen in **Figure 21**, it was demonstrated that the cells could indeed be rotated using the pump in the microvortex. However, the problem was that the sensor was acting erratic in terms of its readings and it was decided that a test of the actual flow rates obtained for specific input pressures used to rotate cells would be performed. This would help determine if the 0.4-7 µL/min sensing region would suffice for the cell rotation applications and also gauge the linear velocities that would be needed for cell rotation. In addition, it would allow accurate changes in chip dimensions and volumetric flow rates while maintaining the linear velocity constant in the future.

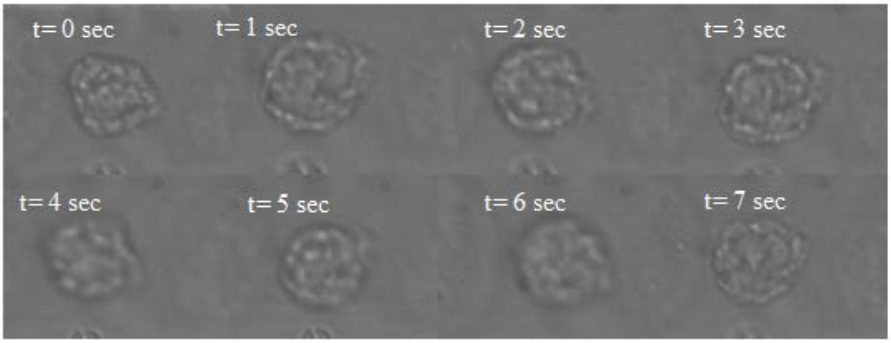

Figure 21: Cell rotation demonstration

For the purpose of the test, collection tubes were used whose weights were measured after collecting for 10 minutes at each set pressure value. Figure 21 has the cell rotating at a set pressure of 100 mbar. This coincided with 50 µL/min on the test and it was found that for cell rotation, it was necessary to have a flow rate of about 25-200 µL/min, with the current chip configuration. Measurements done in the flow control mode confirmed these results, since the sensor would top out in the few tens of mbar range. This information helped determine that higher range sensors were needed for this application with the large (3mm) channel dimensions.

4.2 Rotation characterization data

A series of experiments were performed to obtain relationships between cell rotation and flow rates required to produce these rotations. For the 3 mm wide channel, it was determined the slowest flow rate required for initiating cell rotation (even if intermittent), the flow rate required to produce continuous (if not the most stable) cell rotation and the maximum flow rate that could be used before the cell was ejected out of the recirculatory flow in the microvortex. For all these experiments, a flow sensor capable of reading in the 1-50 µL/min range was used. In addition, the optical trapping laser was used at maximum intensity i.e. 1010 mA (~ 300-400 mW). For the fastest flow rate determination, readings were saturated at 50 µL/min for all widths since that was the sensor's upper limit (0.5, 0.6, 0.5 and 0.75 rev/s being the rotation rates for the respective

trapezoids). **Table 3** shows the rotation characterization data obtained from these experiments.

Table 3: **Rotation characterization data for different flow rates**

Trap opening neck width (µm)	Slowest flow rate (µL/min)	Rotation rate (rev/s)	Stable flow rate (µL/min)	Rotation rate (rev/s)
50	3-8	0.11-0.18	10-18	0.2-0.4
60	4-8	0.11-0.18	10-18	0.2-0.3
70	6-8	0.125-0.15	12-18	0.2-0.4
80	8-10	0.125-0.2	15-25	0.25-0.55

Slowest flow rate: Minimum rate required to initiate rotation

Stable flow rate: Flow rate at which rotation becomes regular (may not be the most stable always)

5. CONCLUSIONS AND FUTURE WORK

5.1 Important contributions

The work in this thesis has optimized the microfabrication of the microfluidic chips needed for single cell rotation using a hydrodynamic microvortex. The process parameters for the earlier, backside diffuser lithography (BDPL) method were optimized to improve the yield, reliability and reproducibility. This process was shown to work with both, SU-8 and KMPR photoresists at different exposure doses. A tilted/inclined exposure technique was adopted to replace the BDPL method to improve the time efficiency and circumvent problems such as non-flat bottoms on the trapezoidal features and unswept volume owing to the diffuser's scattering of light at the same angle in all directions. The backside tilted lithography technique also showed the ability to manipulate the side wall angles down to 52º in air and down to 19º if the setup was immersed in a glycerol bath.

A PDMS-PDMS demolding technique was utilized to overcome the problems with peeling off the PDMS bonded cover glass features from the wafer. By providing a flexible surface from which to peel the cover glass off, this technique improved the yield to 100% from 20-40%. Although it took more time in the first cycle, once a PDMS mold was made, it could be reused an infinite number of times, in theory. It was demonstrated that this technique could produce features at each step that exactly, but in opposite polarity, replicated its predecessor.

A new pump-sensor setup was procured which demonstrated the ability to perform flow-rate/closed-loop controlled rotation of cells, in addition to the normal pressure-driven mode.

5.2 Functional cell-CT

The goal of the project is to be able to perform functional cell-CT using time series and z-series imaging of rotating cells. This would involve using the confocal module of the microscope which uses the Prairie SFC/piezo assembly to allow the QuantEM camera to take images of the fluorescently labeled cells while they are spinning in the microvortex. Functional information can be extracted once there are enough projection data sets of the cell of interest. This will allow analysis of cell morphology while it spins about an axis perpendicular to the optical axis for several minutes to hours. As a result, true 3-D reconstruction imaging of cells can be achieved at nanometer scale resolution, in all axes. SCA -omics can then be performed on particularly interesting live cells and functional images obtained using the method of hydrodynamic rotation of cells in a microvortex.

5.3 Optical tweezers heat generation

It has been shown (Peterman, Gittes, and Schmidt 2003) that while the absorption of light and consequent heat generation is lesser at the wavelength of 1064 nm compared to most lower IR wavelengths, the problem is heating of the surrounding medium due to the light absorption. Heavy water could be used instead of normal DI water, to reduce the absorption co-efficient by two orders of magnitude as compared to normal water (Dholakia and Reece 2006) When using 100 mW laser tweezers (1064 nm in

wavelength), the trap-induced temperature increase is between 1-2 ºC. For human sperm cells, an increase of 10ºC/W of trapping power (approximately 400 mW in this case) has been reported previously (Liu et al. 1995) (Peterman et al. 2003). To prevent direct interaction between photons and cells, particles can be attached to cells and then the laser can be made to strike and trap these particles, rather than the cells themselves. Although this will not stop the surrounding medium from heating up, it will prevent any direct interaction of the cell and light photons, hence reducing the amount of photo damage significantly and increasing viability of the cells. Alternatively, divergent optical beams rather than a single highly focused beam can be used to reduce the photo damage to the cells. Different cells and cell lines will have different absorption coefficients and so it is important to remember that they will absorb and hence react to the same amount of trap power in different ways, irrespective of the surrounding medium. A technique using a standard fluorescence microscope and a CCD camera to measure the temperature dependent fluorescence of a readily available dye such as rhodamine B (temperature dependent between 0 and 100 ºC, making it a useful probe) and can help measure temperature changes based on a reference temperature. This method of fluorescence-based thermometry can measure temperature variations with a precision between 2.4-3.5 ºC (Ross, Gaitan, and Locascio 2001).

5.4 Manifold for chip holding

A manifold for holding the chip to be imaged could help provide more stability to the imaging set-up. This would prevent the fragile cover glass from breaking while also providing for a slit at the bottom to allow for imaging through the bottom objective.

5.5 Microfabrication developments

It would be interesting to find out whether the relationships between cell rotation rate and flow rate differ for different sidewall angles. It is important to evaluate if there is a more stable recirculation and hence stable axis of rotation for the cell. By obtaining the perfect microvortex after experimenting with the sidewall angles at different aspect ratios, it may well be possible to use very little or no laser power at all for trapping the cell, because the microvortex will self-stabilize the cell's rotation, once the cell is in its center. The chip dimensions can be made smaller to the point that just one cell is flown in through the channel, spun and imaged, and finally retrieved for downstream molecular profiling. A diversion channel could be made to hold cells in before optical tweezers are used to bring just the one cell in for processing purposes.

The use of a polymer like COC, as explained in Chapter 2 to bond to PDMS mold would give an added flexibility to the apparatus, completely overcoming disadvantages of the cover glass, while retaining its optical properties suitable for high quality imaging.

Different methods of chemically treating the polymer in order to obtain good adhesion between the two layers would need to be explored.

5.6 Summary of work completed

In this thesis the optimization of microfabrication, its auxiliary processes, and regular, stable cell rotation were successfully demonstrated. In addition, characterization of the cell rotation for chambers with various aspect ratios was also accomplished. This will allow us to obtain live cell CT images and gain insight into live cell dynamics to better understand the underlying mechanisms of disease.

REFERENCES

Aran, Kiana, Lawrence a Sasso, Neal Kamdar, and Jeffrey D Zahn. 2010. “Irreversible, Direct Bonding of Nanoporous Polymer Membranes to PDMS or Glass Microdevices.” *Lab on a Chip* 10 (5) (March 7): 548–52. doi:10.1039/b924816a. http://www.ncbi.nlm.nih.gov/pubmed/20162227.

Ashkin, A. 1970. “0~ 0 0 0” (4): 24–27.

Avery, Simon V. 2006. “Microbial Cell Individuality and the Underlying Sources of Heterogeneity.” *Nature Reviews. Microbiology* 4 (8) (August): 577–87. doi:10.1038/nrmicro1460.

Baek, Sunghoon, and Simon Song. 2011. “A One-step Photolithography Method for Fabrication of a Staggered Herringbone Mixer Using Inclined UV Lithography.” *Journal of Micromechanics and Microengineering* 21 (7) (July 1): 077001. doi:10.1088/0960-1317/21/7/077001. http://stacks.iop.org/0960-1317/21/i=7/a=077001?key=crossref.f4334fba261d699a59d1034b57c1ce8a.

Berthold, A, P M Sarro, and M J Vellekoop. “Two-step Glass Wet-etching for Micro-fluidic Devices”: 613–616.

Beuret, C, A Racine, and Swiss Centre. 2007. “Microfabrication of 3D Multidirectional Inclined Structures By”: 81–85.

Bingelyte, V., J. Leach, J. Courtial, and M. J. Padgett. 2003. “Optically Controlled Three-dimensional Rotation of Microscopic Objects.” *Applied Physics Letters* 82 (5): 829. doi:10.1063/1.1544067. http://link.aip.org/link/APPLAB/v82/i5/p829/s1&Agg=doi.

Chang, Sung-il, and Jun-bo Yoon. 2004. “Arrays Fabricated by a 3D Diffuser Lithography” 12 (25): 6366–6371.

Chao, Shih-Hui, Mark R Holl, Sarah C McQuaide, Timothy T H Ren, Steven a Gales, and Deirdre R Meldrum. 2007. “Phosphorescence Lifetime Based Oxygen Micro-sensing Using a Digital Micromirror Device.” *Optics Express* 15 (17) (August 20): 10681–9. http://www.ncbi.nlm.nih.gov/pubmed/19547422.

Chao, Tzu-Chiao, and Alexandra Ros. 2008. “Microfluidic Single-cell Analysis of Intracellular Compounds.” *Journal of the Royal Society, Interface / the Royal Society* 5 Suppl 2 (October) (October 6): S139–50. doi:10.1098/rsif.2008.0233.focus. http://www.pubmedcentral.nih.gov/articlerender.fcgi?artid=2706030&tool=pmcentrez&rendertype=abstract.

Chiu, Daniel T. 2007. “Cellular Manipulations in Microvortices.” *Analytical and Bioanalytical Chemistry* 387 (1) (January): 17–20. doi:10.1007/s00216-006-0611-2. http://www.ncbi.nlm.nih.gov/pubmed/16955264.

Cohen, a a, N Geva-Zatorsky, E Eden, M Frenkel-Morgenstern, I Issaeva, a Sigal, R Milo, et al. 2008. “Dynamic Proteomics of Individual Cancer Cells in Response to a Drug.” *Science (New York, N.Y.)* 322 (5907) (December): 1511–6. doi:10.1126/science.1160165.

Cortese, Barbara, Matt C. Mowlem, and Hywel Morgan. 2011. “Characterisation of an Irreversible Bonding Process for COC–COC and COC–PDMS–COC Sandwich Structures and Application to Microvalves.” *Sensors and Actuators B: Chemical* 160 (1) (December): 1473–1480. doi:10.1016/j.snb.2011.07.040. http://linkinghub.elsevier.com/retrieve/pii/S0925400511006824.

Cortese, Katia, Alberto Diaspro, and Carlo Tacchetti. 2009. “Advanced Correlative Light/electron Microscopy: Current Methods and New Developments Using Tokuyasu Cryosections.” *The Journal of Histochemistry and Cytochemistry : Official Journal of the Histochemistry Society* 57 (12) (December): 1103–12. doi:10.1369/jhc.2009.954214. http://www.pubmedcentral.nih.gov/articlerender.fcgi?artid=2778083&tool=pmcentrez&rendertype=abstract.

Cotte, Yann, Fatih Toy, Pascal Jourdain, Nicolas Pavillon, Daniel Boss, Pierre Magistretti, Pierre Marquet, and Christian Depeursinge. 2013. “Marker-free Phase Nanoscopy” 7 (February): 113–118. doi:10.1038/NPHOTON.2012.329. http://dx.doi.org/10.1038/nphoton.2012.329.

Dholakia, Kishan, and Peter Reece. 2006. “Optical Micromanipulation Takes Hold Light Can Influence the Motion of Particles , from the Size of a Single Cell Forefront of Many Studies in the Natural Sciences .” 1 (1): 18–27.

Doh, Il, and Young-Ho Cho. 2005. “A Continuous Cell Separation Chip Using Hydrodynamic Dielectrophoresis (DEP) Process.” *Sensors and Actuators A: Physical* 121 (1) (May): 59–65. doi:10.1016/j.sna.2005.01.030. http://linkinghub.elsevier.com/retrieve/pii/S0924424705000464.

Fauver, Mark, Eric Seibel, J Richard Rahn, Michael Meyer, Florence Patten, Thomas Neumann, and Alan Nelson. 2005. “Three-dimensional Imaging of Single Isolated Cell Nuclei Using Optical Projection Tomography.” *Optics Express* 13 (11) (May 30): 4210–23. http://www.ncbi.nlm.nih.gov/pubmed/19495335.

Gao, Weimin, Weiwen Zhang, and Deirdre R Meldrum. 2011. “RT-qPCR Based Quantitative Analysis of Gene Expression in Single Bacterial Cells.” *Journal of Microbiological Methods* 85 (3) (June): 221–7. doi:10.1016/j.mimet.2011.03.008. http://www.ncbi.nlm.nih.gov/pubmed/21440012.

Gosse, Charlie, and Vincent Croquette. 2002. “Magnetic Tweezers: Micromanipulation and Force Measurement at the Molecular Level.” *Biophysical Journal* 82 (6) (June): 3314–29. doi:10.1016/S0006-3495(02)75672-5. http://www.pubmedcentral.nih.gov/articlerender.fcgi?artid=1302119&tool=pmcentrez&rendertype=abstract.

Hou, L, J Zhang, N Smith, J Yang, and J Heikenfeld. 2010. “A Full Description of a Scalable Microfabrication Process for Arrayed Electrowetting Microprisms.” *Journal of Micromechanics and Microengineering* 20 (1) (January): 015044. doi:10.1088/0960-1317/20/1/015044.

Hsu, Chia-Hsien, Dino Di Carlo, Chihchen Chen, Daniel Irimia, and Mehmet Toner. 2008. “Microvortex for Focusing, Guiding and Sorting of Particles.” *Lab on a Chip* 8 (12) (December): 2128–34. doi:10.1039/b813434k. http://www.ncbi.nlm.nih.gov/pubmed/19023476.

Hung, Kuo-Yung, Heng-Tsang Hu, and Fan-Gang Tseng. 2004. “Application of 3D Glycerol-compensated Inclined-exposure Technology to an Integrated Optical Pick-up Head.” *Journal of Micromechanics and Microengineering* 14 (7) (July 1): 975–983. doi:10.1088/0960-1317/14/7/019. http://stacks.iop.org/0960-1317/14/i=7/a=019?key=crossref.ff7e807f0ee1ee87ef298b6014f7a0ee.

Kreysing, Moritz K, Tobias Kießling, Anatol Fritsch, Jochen R Guck, A K Josef, Carl Zeiss, and Microimaging Gmbh. 2008. “The Optical Cell Rotator Abstract :” 16 (21): 912–914.

Lidstrom, Mary E, and Deirdre R Meldrum. 2003. “Life-on-a-chip.” *Nature Reviews. Microbiology* 1 (2) (November): 158–64. doi:10.1038/nrmicro755. http://www.ncbi.nlm.nih.gov/pubmed/15035045.

Lim, David S. W., J. Patrick Shelby, Jason S. Kuo, and Daniel T. Chiu. 2003. “Dynamic Formation of Ring-shaped Patterns of Colloidal Particles in Microfluidic Systems.” *Applied Physics Letters* 83 (6): 1145. doi:10.1063/1.1600532.

Lin, Cheng Ming, Yu Shang Lai, Hsin Ping Liu, Chang Yu Chen, and Andrew M Wo. 2008. “Trapping of Bioparticles via Microvortices in a Microfluidic Device for Bioassay Applications Trapping of Bioparticles via Microvortices in a Microfluidic Device for Bioassay Applications.”

Liu, Y, D K Cheng, G J Sonek, M W Berns, C F Chapman, and B J Tromberg. 1995. “Evidence for Localized Cell Heating Induced by Infrared Optical Tweezers.” *Biophysical Journal* 68 (5) (May): 2137–44. doi:10.1016/S0006-3495(95)80396-6. http://www.pubmedcentral.nih.gov/articlerender.fcgi?artid=1282119&tool=pmcentrez&rendertype=abstract.

Losick, Richard, and Claude Desplan. 2008. “Stochasticity and Cell Fate.” *Science (New York, N.Y.)* 320 (5872) (April): 65–8. doi:10.1126/science.1147888.

Luo, L W, C Y Teo, W L Ong, K C Tang, L F Cheow, and L Yobas. 2007. “Rapid Prototyping of Microfluidic Systems Using a Laser-patterned Tape.” *Journal of Micromechanics and Microengineering* 17 (12) (December): N107–N111. doi:10.1088/0960-1317/17/12/N02.

Miao, Qin, Anthony P Reeves, Florence W Patten, and Eric J Seibel. 2012. “Multimodal 3D Imaging of Cells and Tissue, Bridging the Gap Between Clinical and Research Microscopy.” *Annals of Biomedical Engineering* 40 (2) (February): 263–76. doi:10.1007/s10439-011-0411-5. http://www.ncbi.nlm.nih.gov/pubmed/21984512.

Miltenyi, S, W Müller, W Weichel, and a Radbruch. 1990. “High Gradient Magnetic Cell Separation with MACS.” *Cytometry* 11 (2) (January): 231–8. doi:10.1002/cyto.990110203. http://www.ncbi.nlm.nih.gov/pubmed/1690625.

Molter, Timothy W, Sarah C McQuaide, Mark R Holl, Deirdre R Meldrum, Joseph M Dragavon, Judith B Anderson, a Cody Young, Lloyd W Burgess, and Mary E Lidstrom. 2008. “A New Approach for Measuring Single-Cell Oxygen Consumption Rates.” *IEEE Transactions on Automation Science and Engineering : a Publication of the IEEE Robotics and Automation Society* 5 (1) (January 1): 32–42. http://www.pubmedcentral.nih.gov/articlerender.fcgi?artid=2971563&tool=pmcentrez&rendertype=abstract.

Nandakumar, Vivek, Laimonas Kelbauskas, Roger Johnson, and Deirdre Meldrum. 2011. “Quantitative Characterization of Preneoplastic Progression Using Single-cell Computed Tomography and Three-dimensional Karyometry.” *Cytometry. Part A : the Journal of the International Society for Analytical Cytology* 79 (1) (January): 25–34. doi:10.1002/cyto.a.20997. http://www.pubmedcentral.nih.gov/articlerender.fcgi?artid=3068856&tool=pmcentrez&rendertype=abstract.

Neuman, Keir C., Edmund H. Chadd, Grace F. Liou, Keren Bergman, and Steven M. Block. 1999. “Characterization of Photodamage to Escherichia Coli in Optical Traps.” *Biophysical Journal* 77 (5) (November): 2856–2863. doi:10.1016/S0006-3495(99)77117-1. http://linkinghub.elsevier.com/retrieve/pii/S0006349599771171.

Nilsson, J, M Evander, B Hammarström, and T Laurell. 2009. “Review of Cell and Particle Trapping in Microfluidic Systems.” *Analytica Chimica Acta* 649 (2) (September 7): 141–57. doi:10.1016/j.aca.2009.07.017. http://www.ncbi.nlm.nih.gov/pubmed/19699390.

O’Shea, D C, and W S Rockward. 1995. “Gray-scale Masks for Diffractive-optics Fabrication: II. Spatially Filtered Halftone Screens.” *Applied Optics* 34 (32) (November 10): 7518–26. http://www.ncbi.nlm.nih.gov/pubmed/21060626.

Peterman, Erwin J G, Frederick Gittes, and Christoph F Schmidt. 2003. “Laser-induced Heating in Optical Traps.” *Biophysical Journal* 84 (2 Pt 1) (February): 1308–16. doi:10.1016/S0006-3495(03)74946-7.

Petit, Tristan, Li Zhang, Kathrin E Peyer, Bradley E Kratochvil, and Bradley J Nelson. 2012. “Selective Trapping and Manipulation of Microscale Objects Using Mobile Microvortices.” *Nano Letters* 12 (1) (January 11): 156–60. doi:10.1021/nl2032487. http://www.ncbi.nlm.nih.gov/pubmed/22111870.

Ross, D, M Gaitan, and L E Locascio. 2001. “Temperature Measurement in Microfluidic Systems Using a Temperature-dependent Fluorescent Dye.” *Analytical Chemistry* 73 (17) (September): 4117–23.

Le Saux, B, B Chalmond, Y Yu, a Trouvé, O Renaud, and S L Shorte. 2009. “Isotropic High-resolution Three-dimensional Confocal Micro-rotation Imaging for Non-adherent Living Cells.” *Journal of Microscopy* 233 (3) (March): 404–16. doi:10.1111/j.1365-2818.2009.03128.x. http://www.ncbi.nlm.nih.gov/pubmed/19250461.

Shao, Guocheng, Jiahao Wu, Ziliang Cai, and Wanjun Wang. 2012. “Fabrication of Elastomeric High-aspect-ratio Microstructures Using Polydimethylsiloxane (PDMS) Double Casting Technique.” *Sensors and Actuators A: Physical* 178 (May): 230–236. doi:10.1016/j.sna.2012.01.034. http://linkinghub.elsevier.com/retrieve/pii/S0924424712000581.

Shelby, J Patrick, and Daniel T Chiu. 2004. “Controlled Rotation of Biological Micro- and Nano-particles in Microvortices.” *Lab on a Chip* 4 (3) (June): 168–70. doi:10.1039/b402479f.

De Souza, Natalie. 2011. “Single-cell Methods.” *Nature Methods* 9 (1) (December 28): 35–35. doi:10.1038/nmeth.1819. http://www.nature.com/doifinder/10.1038/nmeth.1819.

Spiegelhalter, Coralie, Valérie Tosch, Didier Hentsch, Marc Koch, Pascal Kessler, Yannick Schwab, and Jocelyn Laporte. 2010. “From Dynamic Live Cell Imaging to 3D Ultrastructure: Novel Integrated Methods for High Pressure Freezing and Correlative Light-electron Microscopy.” *PloS One* 5 (2) (January): e9014. doi:10.1371/journal.pone.0009014. http://www.pubmedcentral.nih.gov/articlerender.fcgi?artid=2815783&tool=pmcentrez&rendertype=abstract.

Suleski, T J, and D C O’Shea. 1995. “Gray-scale Masks for Diffractive-optics Fabrication: I. Commercial Slide Imagers.” *Applied Optics* 34 (32) (November 10): 7507–17. http://www.ncbi.nlm.nih.gov/pubmed/21060625.

Tait, Stephen W G, and Douglas R Green. 2010. “Mitochondria and Cell Death: Outer Membrane Permeabilization and Beyond.” *Nature Reviews. Molecular Cell Biology* 11 (9) (September): 621–32. doi:10.1038/nrm2952. http://www.ncbi.nlm.nih.gov/pubmed/20683470.

Yu, Y, a Trouvé, B Chalmond, O Renaud, and S L Shorte. 2011. “Confocal Bi-protocol: a New Strategy for Isotropic 3D Live Cell Imaging.” *Journal of Microscopy* 242 (1) (April): 70–85. doi:10.1111/j.1365-2818.2010.03440.x. http://www.ncbi.nlm.nih.gov/pubmed/21128940.

Yun, Hoyoung, Kisoo Kim, and Won Gu Lee. 2013. “Cell Manipulation in Microfluidics.” *Biofabrication* 5 (2) (June): 022001. doi:10.1088/1758-5082/5/2/022001. http://www.ncbi.nlm.nih.gov/pubmed/23403762.

Yun, M. H. 1998. “Analysis of KOH Etching of (100) Silicon on Insulator for the Fabrication of Nanoscale Tips.” *Journal of Vacuum Science & Technology B: Microelectronics and Nanometer Structures* 16 (5) (September): 2844. doi:10.1116/1.590282. http://link.aip.org/link/?JVB/16/2844/1&Agg=doi.

Zanacchi, Francesca Cella, Zeno Lavagnino, Michela Perrone Donnorso, Alessio Del Bue, Laura Furia, Mario Faretta, and Alberto Diaspro. 2011. “Resolution Imaging in Thick Biological Samples” 8 (12): 1047–1050. doi:10.1038/NMETH.1744.

Zeng, Jia, Jiangxin Wang, Weimin Gao, Aida Mohammadreza, Laimonas Kelbauskas, Weiwen Zhang, Roger H Johnson, and Deirdre R Meldrum. 2011. “Quantitative Single-cell Gene Expression Measurements of Multiple Genes in Response to Hypoxia Treatment.” *Analytical and Bioanalytical Chemistry* 401 (1) (July): 3–13. doi:10.1007/s00216-011-5084-2.

Zhang, Hu, and Kuo-Kang Liu. 2008. “Optical Tweezers for Single Cells.” *Journal of the Royal Society, Interface / the Royal Society* 5 (24) (July 6): 671–90. doi:10.1098/rsif.2008.0052. http://www.pubmedcentral.nih.gov/articlerender.fcgi?artid=2408388&tool=pmcentrez&rendertype=abstract.